J. Fluid Mech. (2013), *vol.* 729, *pp.* 603–637. © Cambridge University Press 2013
doi:10.1017/jfm.2013.326

DNS of a turbulent boundary layer with surface roughness

James Cardillo[1], Yi Chen[1], Guillermo Araya[3],†, Jensen Newman[2,3], Kenneth Jansen[4] and Luciano Castillo[3]

[1]Department of Mechanical, Aerospace, and Nuclear Engineering, Rensselaer Polytechnic Institute, Troy, NY 12180, USA

[2]Department of Mathematical Sciences, Rensselaer Polytechnic Institute, Troy, NY 12180, USA

[3]Department of Mechanical Engineering, Texas Tech University, Lubbock TX 79401, USA

[4]University of Colorado at Boulder, Boulder, CO 80309, USA

(Received 3 August 2012; revised 6 May 2013; accepted 19 June 2013; first published online 24 July 2013)

A pioneer direct numerical simulation (DNS) of a turbulent boundary layer at $Re_\theta = 2077$–2439, was performed, on a rough surface and with a zero pressure gradient (ZPG). The boundary layer was subjected to transitional, 24-grit sandpaper surface roughness, with a roughness parameter of $k^+ \simeq 11$. The computational method involves a synergy of the dynamic multi-scale approach devised by Araya *et al.* (2011) for prescribing inlet turbulent boundary conditions and a new methodology for mapping high-resolution topographical surface data into a computational fluid dynamics (CFD) environment. It is shown here that the dynamic multi-scale approach can be successfully extended to simulations which incorporate surface roughness. The DNS results demonstrate good agreement with the laser Doppler anemometry (LDA) measurements performed by Brzek *et al.* (2008) and Schultz & Flack (2003) under similar conditions in terms of mean velocity profiles, Reynolds stresses and flow parameters, such as the skin friction coefficient, boundary and momentum thicknesses. Further, it is demonstrated that the effects of the surface roughness on the Reynolds stresses, at the values of $Re_\theta = 2077$–2439, are scale-dependent. Roughness effects were mainly manifested up to $y/\delta \approx 0.1$. Generally speaking, it was observed that inner peak values of Reynolds stresses increased when considering outer units. However, decreases were seen in inner units. In the outer region, the most significant differences between the present DNS smooth and rough cases were computed in the wall-normal component $\langle v'^2 \rangle$ of the Reynolds stresses and in the Reynolds shear stresses $\langle u'v' \rangle$ in outer units. From the resulting flow fields a proper orthogonal decomposition (POD) analysis is performed and the effects of the surface roughness are distinctly observed in the most energetic POD modes. The POD analysis shows that the surface roughness causes a redistribution of the kinetic energy amongst the POD modes with energy being shifted from low-order to high-order modes in the rough case versus the smooth case. Also, the roughness causes a marked decrease in the characteristic wavelengths observed in the POD modes, particularly in the streamwise component of the velocity field. Low-order modes of the streamwise component demonstrated characteristic wavelengths of the order of

† Email address for correspondence: araya@mailaps.org

https://doi.org/10.1017/jfm.2013.326 Published online by Cambridge University Press

3δ in the smooth case, whereas the same modes for the rough case demonstrated characteristic wavelengths of only δ.

Key words: boundary layers, turbulence modelling, turbulence simulation

1. Introduction

Turbulent boundary layers play an essential role in science and engineering. They are not an exception: they are the norm. Due to their importance, it is no surprise that turbulent boundary layers have been studied extensively for more than 70 years. Over the past few decades, the field of computational fluid dynamics has gone through several advancements; however, simulations of spatially developing turbulent boundary layers remain a computational challenge because of the complicated nature of prescribing turbulent inflow boundary conditions. The steep computational demands of simulating such flows increases with the addition of other complex external conditions, including pressure gradients, surface roughness, thermal fields, and free stream turbulence (to name a few). Hence, simulations of spatially developing turbulent boundary layers incorporating surface roughness are scarce. Most flows in modern science and engineering involve some type of irregular or roughened surface. Flows around surfaces such as an iced aeroplane wing, the hull of a submarine covered by barnacles and other crustaceans, turbine blades shrouded with the splattered remains of insects, materials with a rough granular surface finish, or land blanketed with trees and buildings – all involve surface roughness. Consequently, there is a growing need relevant to engineering applications for simulations of spatially developing turbulent boundary layers over roughened surfaces to accompany the myriad of experiments on the subject.

Experiments on pipe flows with uniform sand grit roughness can be seen as early as Nikuradse (1933). For years to follow, many investigators, such as Hama (1945), Clauser (1954), Rotta (1960), Perry & Jourbert (1963) and Schlichting (1979), and as recently as Raupach (1991) have used a log law approach to characterize the flow field of the rough surface turbulent boundary layer. In the log law approach, a single parameter was adjusted to accommodate 'd-type' and 'k-type' roughnesses. The k-type roughness represents surfaces given by sand grain surfaces, whereas the d-type roughness is characterized by two-dimensional geometry, mainly rectangular geometries. It was later found that factors such as the spacing and the shape of the roughness also affected this parameter. Townsend (1976) devised the 'attached-eddy hypothesis' which stated that all of the structures and energy components of the turbulent boundary layer were independent of viscosity and surface roughness – which caused a great deal of controversy. Later, Perry, Lim & Henbest (1987) demonstrated that at high Reynolds numbers, the rough surface turbulent boundary layer was structurally similar to the smooth surface turbulent boundary layer. Recent experimental studies performed by Kunkel & Marusic (2006) at extremely high Reynolds numbers provided evidence that supported the earlier wall similarity hypothesis for both smooth and rough boundary layers. Schultz & Flack (2007) performed experiments spanning a wide range of roughness regimes and Reynolds numbers ($Re_\theta = 2180$–$21\,700$, $k^+ = 0$–26). In their study, they compared the results of smooth and rough surface turbulent boundary layers. Their results provided convincing support for the wall similarity hypothesis of Townsend (1976) and Raupach (1991).

https://doi.org/10.1017/jfm.2013.326 Published online by Cambridge University Press

Schultz & Flack (2007) concluded that there was a large separation of scales between the outer layer of the boundary layer and the surface roughness; therefore, the outer layer was unaffected by the presence of the roughness. However, it was hypothesized that if the separation of scales was not large, or the roughness was two-dimensional in nature, the outer layer could be affected by the surface roughness. Also, Brzek *et al.* (2008) performed experiments on the turbulent boundary layer with a sand grit surface roughness distribution similar to the conditions of Schultz & Flack (2007). Brzek *et al.* (2008) described a meso-layer connecting the inner and outer layers of the boundary layer and concluded that this layer dictates the communication between the inner and outer layers. Their assertion was that when the Reynolds number is low, viscous stresses can be found in the meso-layer which propagate to the outer region of the boundary layer. As the Reynolds number becomes higher, the meso-layer becomes smaller and the overlap/wake region increases. Consequently, this communication of scales between the inner and outer layers is inhibited, and one observes a much smaller dependence of the skin friction on the Reynolds number. Further evidence of minimal effect of surface roughness on the outer flow at high Reynolds number were also recently supported by Krogstad & Efros (2012). Here, they showed that for a boundary layer over spanwise square rods, the effects of the roughness on the outer flow is greatly diminished when the Reynolds number is increased (up to $Re_\theta = 32\,600$ in their experiments). Studies such as these have led to the controversial assertion that roughness effects could not be seen in the outer layer of the boundary layer. Contrary to this point, Krogstad, Antonia & Browne (1992) showed that in the outer layer of the boundary layer, the structures of turbulence were different from those of the smooth wall boundary layer at $Re_\theta = 12\,800$. Similarly, Leonardi *et al.* (2003) performed a direct numerical simulation (DNS) of a channel flow at a range of Reynolds numbers ($Re_h = 4200$–$10\,400$, based on the channel half-height h) which showed that roughness effects could be seen in the outer region of the turbulent boundary layer. This observation was also reported in studies by Cal *et al.* (2009) and Brzek *et al.* (2008). Recently, Hong, Katz & Schultz (2011) performed accurate measurements in a turbulent channel flow at $Re_\tau = 3520$–5360 with three-dimensional roughness elements, and demonstrated that the instantaneous small-scale structures near the rough wall were lifted up away from the wall rapidly by the larger-scale structures, allowing the roughness to affect the outer flow, contradicting Townsend's hypothesis that effects of roughness are confined near the surface. Jiménez (2004) argued that the contradictory views of these investigators were due to the ratio of the roughness height to the boundary layer thickness, k/δ, which essentially dictates how far the roughness elements protrude into the boundary layer. Jiménez (2004) asserted that if the roughness was small compared to the boundary layer thickness, $k/\delta < 1/50$, the wall similarity hypothesis was verified. However, Brzek *et al.* (2008) argued that in addition to this requirement, the momentum thickness Reynolds number must be greater than 10 000 (where a true overlap exists, i.e. for $Re_\theta > 10\,000$). Then, under these conditions one should expect that Townsend's hypothesis is valid.

It is evident that the contradicting points of view discussed thus far do not provide a satisfactory conclusion to the question of outer layer similarity in the rough surface turbulent boundary layer. The present work attempts to advance the field by developing tools to be used in the research of the rough turbulent boundary layer by providing a methodology to perform computationally feasible direct numerical simulations of a turbulent boundary layer with surface roughness at relatively moderate Reynolds numbers. DNS has the ability to solve the full Navier–Stokes equations with great accuracy for all the scales in the turbulent boundary layer. Hence, DNS

https://doi.org/10.1017/jfm.2013.326 Published online by Cambridge University Press

has the potential to address the fundamental problem of outer layer similarity. The complication with DNS lies in its steep computational demands. Performing a DNS of a spatially developing turbulent boundary layer requires extensive computational power to resolve the spectrum of scales, and involves the need to prescribe time-dependent inlet boundary conditions. Adding surface roughness to the mix increases the computational overhead further, as the complex characteristics of the surface geometry must be fully recreated in a computational environment. There have been numerous attempts to simulate rough surface turbulent boundary layers using turbulence models; however, direct numerical simulations on the topic are quite scarce. Few successful attempts have been carried out using DNS which incorporates sand grit surface roughness. A DNS was performed by Scotti (2007) which incorporated an array of small ellipsoids to create a 'virtual' surface in a fully developed channel flow, which reflected the properties of sandpaper, and it was demonstrated that the method was feasible. A numerical simulation of a turbulent boundary layer which models surface roughness using an elliptic relaxation scheme with v^2–f model framework was performed by George *et al.* (2010). These results demonstrated reasonable agreement with laser Doppler velocimetry (LDV) measurements of transitionally rough turbulent boundary layer data, and they indicate that the surface roughness can be understood as a means of redistributing turbulent kinetic energy. George *et al.* (2010) also discuss the length and time scales in the rough wall turbulent boundary layer, and conclude that they are constant within the rough wall, increasing linearly with increasing element height, supporting the earlier hypothesis of Jiménez (2004).

Therefore, the present study aims to provide a pioneer DNS of the rough surface turbulent boundary layer which incorporates actual surface topography into a computational fluid dynamics (CFD) environment. The roughness is not modelled or simplified in any way; rather, it is measured from an actual surface and mapped onto the computational domain. The manuscript is organized as follows: the numerical method and its extension to rough surfaces is described in § 2, the methodology of implementing sand grit surface topography into the present DNS is explained in § 3, the setup and specification of the parameters for the current DNS case is presented in § 4, numerical results in terms of the mean velocity, fluctuations and two-point correlations are reported in § 5, and a brief proper orthogonal decomposition (POD) analysis is shown in § 6. Finally, § 7 articulates the major findings and conclusions of the article.

2. Overview of the dynamic multi-scale approach

The current DNS employs the dynamic multi-scale approach devised by Araya *et al.* (2011) for prescribing turbulent inlet boundary conditions. The dynamic multi-scale approach is based on the classical recycling/rescaling method developed by Lund, Wu & Squires (1998), but uses only a single domain instead of two. In order to achieve a statistically steady flow, computational domains consisted of large boxes with a developing region. These computational domains often had to be very long in the streamwise direction to incorporate transition and only a small amount of the domain contained the fully turbulent flow. The original recycling/rescaling method was developed as a way to eliminate the developing region of the computational domain, therefore reducing the computational costs of simulating spatially evolving boundary layer flows. By introducing a recycling plane into the computational domain, the flow at the recycling plane could be rescaled and re-injected at the inlet plane of the domain. By allowing the flow to follow this recycling, rescaling, and re-injection

https://doi.org/10.1017/jfm.2013.326 Published online by Cambridge University Press

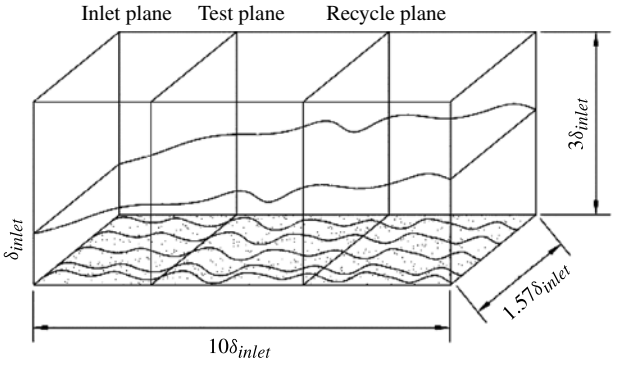


FIGURE 1. Computational domain for the dynamic multi-scale approach.

process, it was found that after some time, the flow would reach a statistically steady state. Thus, the recycling method was advantageous because a smaller, less computationally demanding domain could be used to simulate a turbulent boundary layer. The classical method developed by Lund *et al.* (1998) invoked a single, inner scaling factor at the recycle plane. By introducing a 'test plane' in between the recycling and the inlet planes, as shown in figure 1, the required flow parameters (e.g. inlet friction velocity) at the inlet plane are extrapolated based on the solution downstream. This improvement to the original rescaling/recycling method avoids the need to use some empirical correlations, as in Lund *et al.* (1998). To incorporate surface roughness, a slight modification to the original dynamic multi-scale approach was incorporated and is explained in subsequent sections. However, the full details of the dynamic multi-scale approach are contained in Araya *et al.* (2011).

The dynamic multi-scale approach involves introducing two planes to the computational domain: the recycling plane and the test plane. An illustration of the computational domain with the inlet, test, and recycle planes is shown in figure 1. It is important to note that this methodology also applies to the thermal field with and without pressure gradients (Araya, Jansen & Castillo 2009; Araya *et al.* 2011; Araya & Castillo 2012). The boundary layer at the inlet plane is divided into an inner and an outer region while the instantaneous velocity is divided into a mean velocity, U_i, plus a fluctuating component, u_i'. The basic idea, as described in Araya *et al.* (2011), is to construct a time-dependent velocity field at the inlet separately in the inner (superscript (i)) and outer (superscript (o)) regions, according to

$$u_i(x_{inl}, y, z, t) = \left[(U_i)_{inl}^{(i)} + \left(u_i'\right)_{inl}^{(i)}\right]\{1 - W(\eta)\} + \left[(U_i)_{inl}^{(o)} + \left(u_i'\right)_{inl}^{(o)}\right] W(\eta)\,, \quad (2.1)$$

where $\eta = y/\delta$, and $\delta(x)$ is the boundary layer thickness. The function $W(\eta)$ is a weighting function that goes smoothly from 0 near the wall in the inner region (small $\eta = y/\delta$), to $W(\eta) \to 1$ in the outer region ($\eta \to 1$). For $W(\eta)$ we use the same tanh-profile of Lund *et al.* (1998), namely $W(\eta) = 0.5\{1 + \tanh[\alpha(\eta - b)/((1 - 2b)\eta + b)]/\tanh(\alpha)\}$, where $\alpha = 4$ and $b = 0.2$. Hence, the mean and fluctuating velocities can be specified based on the mean and fluctuating velocities at the recycle plane, but separately for the inner and outer regions (Araya *et al.* 2011).

One of the most important aspects of the dynamic multi-scale approach is the selection of the appropriate scaling law to be used in the re-scaling process. In this investigation, we are using the velocity scaling law (the equilibrium similarity) based

https://doi.org/10.1017/jfm.2013.326 Published online by Cambridge University Press

Variable	Inner		Outer	
	Classical	Equilibrium similarity	Classical	Equilibrium similarity
$\overline{U}, u', w'$	u_τ	u_τ	u_τ	U_∞
$\overline{V}$	U_∞	u_τ	U_∞	$U_\infty \mathrm{d}\delta/\mathrm{d}x$
v'	u_τ	u_τ	u_τ	$U_\infty \mathrm{d}\delta/\mathrm{d}x$
$\langle u'v' \rangle$	u_τ^2	u_τ^2	u_τ^2	$U_\infty^2 \mathrm{d}\delta/\mathrm{d}x$

TABLE 1. Velocity scaling functions.

on the study by George & Castillo (1997) (henceforth GC97). However, the proposed method is designed in such a way that any other scaling law can be implemented. Table 1 depicts the velocity scaling functions considered in the proposed turbulent inflow generation method and the classical scales. The GC97 scaling laws have already been tested in Araya *et al.* (2009, 2011) in the rescaling process with high-quality results. It can be observed that different scales are used by GC97 in the inner and outer regions, contrary to the classical approach, which is based on a single scaling, mainly the friction velocity.

In the inner region, the fluctuating velocities are rescaled by matching the inner height in wall units above the wall between the recycle and inlet planes, and by rescaling the velocities using the friction velocity scale. As stated in Araya *et al.* (2011), the fluctuating velocity in the inner region $\left(u_i'\right)_{inl}^{(i)} \equiv u_i'^{(i)}(x_{inl}, y, z, t)$ at some height y is obtained from the corresponding height at the recycle plane according to

$$u_i'^{(i)}(x_{inl}, y, z, t) = \lambda_{u_j'}^{(i)} u_i'(x_{rec}, \lambda_{u_j'}^{(i)} y, z, t), \quad \text{where } \lambda_{u_j'}^{(i)} = \frac{(u_\tau)_{inl}}{(u_\tau)_{rec}}. \tag{2.2}$$

Here, $u_\tau = \sqrt{\tau_w/\rho}$ is the local friction velocity, τ_w is the wall shear stress, and ρ is the fluid density. A similar relation holds connecting the mean velocity in the inner region, $U^{(i)}(x_{inl}, y) = \lambda_U^{(i)}\ U(x_{rec}, \lambda_U^{(i)} y)$, with a factor $\lambda_U^{(i)}$, also set equal to the ratio of friction velocities. In this study, it can be seen from table 1 that all components of the fluctuating and mean velocities in the equilibrium similarity scale with the friction velocity, and therefore $\lambda_{u_j'}^{(i)} = \lambda_{\bar{U}_j}^{(i)} = (u_\tau)_{inl}/(u_\tau)_{rec} = \lambda_{inner}$, where $j = 1, 2, 3$. Note, however, that in this paper $\bar{U}_3 = 0$.

In the outer region, an outer layer ratio $\lambda^{(o)}$ connects variables between the planes in outer units $y/\delta(x)$. Again from table 1 it may be seen that

$$\lambda_{u_j'}^{(o)} = \lambda_{\bar{U}_j}^{(o)} = \frac{(U_\infty)_{inl}}{(U_\infty)_{rec}} = \lambda_{outer_1}, \quad j = 1, 3 \tag{2.3}$$

and

$$\lambda_{u_j'}^{(o)} = \lambda_{\bar{U}_j}^{(o)} = \frac{(U_\infty)\dfrac{\mathrm{d}\delta}{\mathrm{d}x}_{inl}}{(U_\infty)\dfrac{\mathrm{d}\delta}{\mathrm{d}x}_{rec}} = \lambda_{outer_2}, \quad j = 2. \tag{2.4}$$

The remaining challenge is to specify values for the λ factors. For the current DNS case, all scaling factors for the outer layer of the boundary layer remain unaffected by the roughness. Hence, their calculations remain the same as indicated in Araya

https://doi.org/10.1017/jfm.2013.326 Published online by Cambridge University Press

et al. (2011). However, the scaling factors for the inner layer must be modified to accommodate the surface roughness. Araya *et al.* (2011) obtained a scaling factor for the inner boundary layer by computing the dynamic power law exponent, γ, which is calculated based on the friction velocity, $u_\tau = \sqrt{\nu(\partial U/\partial y)_{y=0}}$, where ν is the kinematic viscosity, U is the streamwise component of the mean velocity, and y is the wall-normal coordinate. In this approach, the friction velocity must be calculated at the test and recycling planes. In the presence of surface roughness, however, the viscous sublayer of the turbulent boundary layer is disturbed, causing the calculation of the friction velocity to become difficult or impossible by traditional means, as stated by Brzek *et al.* (2008). As a result, we have proposed the use of the momentum integral equation to compute λ_{inner} at every time step by assuming a power law variation of the momentum thickness, as follows:

$$\frac{\theta}{x} = CRe_x^{\gamma_\theta}, \tag{2.5}$$

where θ is the momentum thickness, x is the streamwise coordinate, $Re_x = U_\infty x/\nu$ is the streamwise Reynolds number, C is the constant of proportionality, and γ_θ is the dynamic power law exponent. The streamwise coordinate is defined as $x = x' + x_{inl}$, where $x = 0$ indicates the virtual origin of the boundary layer, $x' = 0$ means the computational box origin and x_{inl} is the distance between the virtual origin and the inlet plane. Based on the prescribed inlet boundary layer thickness, x_{inl} has been selected based on the GC97 theory to initiate simulations. Furthermore, the value of x_{inl} has been adjusted during the numerical simulations by curve fitting of $\delta(x)$ (not shown here). However, meaningless changes have been observed in the original value of x_{inl} proposed, without a significant incidence on the computation of γ_θ. Thus, rearranging (2.5), the dynamic power law exponent can be computed based on the momentum thickness ratios and the Reynolds numbers at the test and recycle planes as shown by

$$\gamma_\theta = \frac{\ln[(\theta/x)_{test}/(\theta/x)_{rec}]}{\ln[(Re_x)_{test}/(Re_x)_{rec}]}. \tag{2.6}$$

Notice that in this formulation only flow parameters involving recycling and test planes are necessary. Moreover, according to Araya *et al.* (2011), one assumes that γ_θ is constant along the computational domain between the inlet and recycle planes. For cases where the Reynolds number does not vary greatly, and the flow is in reasonable equilibrium during the downstream evolution, this assumption appears to be warranted. Therefore, to calculate the ratio of friction velocities from the inlet to the recycle planes, $\lambda_{inner} = (u_\tau)_{inl}/(u_\tau)_{rec}$, one employs the momentum integral equation (2.7) for zero pressure gradient (ZPG) flows:

$$\frac{\mathrm{d}\theta}{\mathrm{d}x} = \left(\frac{u_\tau}{U_\infty}\right)^2. \tag{2.7}$$

The momentum thicknesses are computed at each streamwise station by means of the trapezoidal rule as follows:

$$\theta = \int_0^\infty \frac{U}{U_\infty}\left(1 - \frac{U}{U_\infty}\right)\mathrm{d}y \approx \sum_2^{N_y-1} \frac{U_{Aver}}{U_\infty}\left(1 - \frac{U_{Aver}}{U_\infty}\right)(y_i - y_{i-1}), \tag{2.8}$$

where $U_{Aver} = (U_i + U_{i-1})/2$ for $i = 2, (N_y - 1)$ and N_y represents the number of points in the wall-normal direction of the mesh. In addition, the index $i = 1$ indicates the wall

https://doi.org/10.1017/jfm.2013.326 Published online by Cambridge University Press

and $i = 2$ is the first off-wall point in the mesh (i.e. $y_{min} = y_2$), which represents the first integration point. Furthermore, all points in the mesh that fall 'inside' the local roughness height are assigned zero-velocity values. Consequently, these points do not contribute to the momentum thickness computation. It is worth mentioning that $y_1 = 0$ is considered the origin of the vertical axis for the smooth and rough cases, which coincides with the wall for the smooth case.

One can compute the momentum thickness derivative using (2.5), and rearrange (2.7) for the friction velocity, yielding

$$u_\tau = U_\infty \sqrt{CRe_x^{\gamma_\theta}(1+\gamma_\theta)}. \tag{2.9}$$

Thus, (2.9) can be calculated at any streamwise plane, and finally, the factor λ_{inner} reads

$$\lambda_{inner} = \frac{(u_\tau)_{inl}}{(u_\tau)_{rec}} = \sqrt{\left[\frac{(Re_x)_{inl}}{(Re_x)_{rec}}\right]^{\gamma_\theta}}, \tag{2.10}$$

and with (2.10), the inner mean velocity components and the fluctuations can be scaled at the inlet planes using

$$\bar{U}_{inl}^{inner} = \lambda_{inner}\bar{U}_{rec}^{inner}, \tag{2.11}$$
$$\bar{V}_{inl}^{inner} = \lambda_{inner}\bar{V}_{rec}^{inner}, \tag{2.12}$$
$$u'^{inner}_{inl} = \lambda_{inner}u'^{inner}_{rec}, \tag{2.13}$$
$$v'^{inner}_{inl} = \lambda_{inner}v'^{inner}_{rec}, \tag{2.14}$$
$$w'^{inner}_{inl} = \lambda_{inner}w'^{inner}_{rec}, \tag{2.15}$$

with similar relations holding for the outer variables.

Consequently, with the calculation of λ_{inner}, λ_{outer_1} and λ_{outer_2} (the scaling factors for the inner and outer boundary layers) the appropriate scaling of the inner and outer boundary layers at the inlet of the computational domain is determined. As mentioned earlier, the scaling laws used in the proposed inflow generation method are based on the GC97 theory and the results might be influenced by the selected scaling. However, it is worth noting that the dynamic multi-scale approach has been developed in such a way as to apply any other scaling laws from the literature. Hence, the scaling factors for the inner and outer boundary layers can be used to rescale and recycle the entire boundary layer velocity profile at the inlet of the computational domain. This implementation of the recycling method allows the turbulent flow to evolve spatially without simulating the entire transition phase. Therefore, because of the dynamic approach employed here, the spatial evolution of the boundary layer is dynamically computed based on the flow field. Hence, the current method can be extended to simulations with pressure gradients, thermal fields and stratification (Araya *et al.* 2011; Araya & Castillo 2012; Araya, Castillo & Jansen 2013).

3. Surface roughness methodology

The numerical code for performing DNS of the full Navier–Stokes equations is known as PHASTA (parallel hierarchic adaptive stabilized transient analysis). The flow solver PHASTA has been defined by considering a stabilized finite element method in space to spatially discretize the incompressible Navier–Stokes equations with a streamline upwind Petrov–Galerkin (SUPG) stabilization. Furthermore, the

https://doi.org/10.1017/jfm.2013.326 Published online by Cambridge University Press

weak formulation of the problem originates a system of nonlinear ordinary differential equations, which are discretized in time via a generalized-α time integrator generating a nonlinear system of algebraic equations. Further, this system is linearized by Newton's method, which yields a linear algebraic system of equations,

$$\begin{bmatrix} \boldsymbol{K} & \boldsymbol{G} \\ -\boldsymbol{G}^T & \boldsymbol{C} \end{bmatrix} \begin{bmatrix} \Delta\dot{u} \\ \Delta\dot{p} \end{bmatrix} = - \begin{bmatrix} \boldsymbol{R}_m \\ \boldsymbol{R}_c \end{bmatrix}, \tag{3.1}$$

where the matrix $\boldsymbol{K}$ derives from the tangent of the momentum equation with respect to the acceleration, $\boldsymbol{G}$ derives from the tangent of the momentum equation with respect to the pressure time derivative, and $\boldsymbol{C}$ derives from the tangent of the continuity equation with respect to pressure time derivative. The matrices $\boldsymbol{R}_m$ and $\boldsymbol{R}_c$ are the momentum and continuity residuals, respectively. Equation (3.1) can be solved monolithically; however, the required tight tolerance makes this approach almost impractical. Consequently, a more feasible alternative consists of solving approximately a preconditioned system. Thus, the equation for $\Delta\dot{p}$ is obtained by static condensation of (3.1), leading us to the discrete pressure Poisson equation (PPE):

$$\left[\boldsymbol{G}^T\hat{\boldsymbol{K}}^{-1}\boldsymbol{G} + \boldsymbol{C}\right] \Delta\dot{p} = \left[-\boldsymbol{G}^T\hat{\boldsymbol{K}}^{-1}\boldsymbol{R}_m - \boldsymbol{R}_c\right], \tag{3.2}$$

where $\hat{\boldsymbol{K}}^{-1}$ is an approximation of $\boldsymbol{K}^{-1}$ obtained by considering only the diagonal entries of $\boldsymbol{K}^{-1}$. The linear equation system (3.2) is first solved by the conjugate gradient (CG) method. Later, the system of equations (3.1) is computed by the GMRES method. Moreover, the fully coupled momentum and continuity equations are solved with multiple nonlinear iterations (two nonlinear iterations are performed on each step) and an additional discrete pressure Poisson equation between each iteration, to maintain a tight tolerance on the continuity equation (Whiting & Jansen 2001; Sun 2008). Although higher orders of accuracy could be achieved with PHASTA by selecting appropriate elements; in practice, linear elements were used which yielded global second-order accuracy in space. Furthermore, satisfactory results have been achieved with this configuration (Araya *et al.* 2009, 2011; Araya & Castillo 2012).

In all cases, the meshes are structured with hexahedral elements, which show excellent performance in turbulent flow simulations. For the velocity field, the no-slip condition is imposed at the wall; meanwhile at the free stream location, the streamwise velocity is given by U_∞ and zero derivatives of the normal and spanwise velocities. At the outflow plane, the pressure is prescribed (Dirichlet condition) and at the inlet station, the time-dependent inflow conditions for the velocity and temperature fields are generated based on the dynamic multi-scale approach by Araya *et al.* (2011). Periodic boundary conditions are prescribed in the spanwise direction. In the wall-normal direction, non-uniform mesh sizes are used with the mesh properties indicated in table 2. From this table, it may be observed that the smooth and rough cases are very comparable in terms of Reynolds number range. The differences between the two simulations are the spatiotemporal resolution (i.e. $\triangle x^+$, $\triangle y^+$, $\triangle z^+$ and $\triangle t^+$, the sample time and δ^+_{inl}).

In order to characterize the surface roughness, a new subroutine has been added to the PHASTA code. The subroutine employs a 'displaced-boundary' method. It works by taking the no-slip condition, which is originally assigned to the bottom wall of the computational domain, and displacing it to the height of the roughness element at the corresponding node. In other words, the no-slip condition is extended to the height of the roughness elements. The corresponding heights to which the no-slip condition is

https://doi.org/10.1017/jfm.2013.326 Published online by Cambridge University Press

Parameters	ZPG smooth	ZPG rough
Re_θ	1940–2300	2077–2439
L_x	$10\delta_{inl}$	$10\delta_{inl}$
L_y	$3\delta_{inl}$	$3\delta_{inl}$
L_z	$1.57\delta_{inl}$	$1.57\delta_{inl}$
$N_xN_yN_z$	$400 \times 150 \times 125$	$400 \times 150 \times 125$
Δx^+	23	24.6
Δy^+_{min}, Δy^+_{max}	0.5, 25	0.545, 26.74
Δz^+	11	11.77
Δt^+	0.44	0.50
$T_{sample}\dfrac{u_\tau^2}{\nu}$	2640	6500
δ^+_{inl}	980	1048
N_{procs}	128	128

TABLE 2. Table showing proposed DNS cases and domain parameters for smooth and rough ZPG simulations.

displaced at a particular node are determined by implementing actual topographical data of a surface into the computational environment. For the current case, the primitive topographical data (Brzek *et al.* 2008) consists of laser measurements of the surface of 24-grit sandpaper, as shown in figure 2(*a*). By performing a two-point correlation analysis of the roughness height distributions (not shown here), it was determined that heights were almost uncorrelated from a distance of 10 mm in the streamwise and spanwise directions. Therefore, one could think of the 10 mm $\times$ 10 mm sample unit as a single 'brick' which could be used in order to cover the entire floor of the computational domain. The sample units or 'bricks' are mirrored an appropriate amount of times to fill the bottom of the computational box such that the interfaces between neighbouring sample units contain no discontinuities. The resolution of the laser device is 132×666 within a sample unit of 10 mm by 10 mm.

The spectrum of the sample unit is computed using a two-dimensional fast Fourier transform (FFT) and is shown in figure 2(*b*). The FFT allows us to determine which wavelengths of the surface topography contribute the most to the overall spectrum. The white portions of the figure represent wavenumbers which make little to no contribution to the spectrum, and thus are not relevant for the reconstruction of the current surface topography. However, the grey and the dark portions indicate wavenumbers which make substantial contributions to the spectrum. A dot-dashed line is drawn in the figure to show where the most significant contributions to the spectrum lie. One can observe that most of the roughness data lie at wavenumbers less than 2π mm^{-1}. However, the highest contributions are present at wavenumbers less than $6\pi/5 = 3.77$ mm^{-1}. To quantify what percentage of the roughness lies in the darker areas, the standard deviation was computed for the original roughness data, and for roughness with the dark portions filtered out. The standard deviation of the original sample was 250 μm whereas the standard deviation for the filtered roughness was 29 μm. Therefore, we are confident in most of the roughness being captured by the wavenumbers specified above.

In order to perform a fair comparison with the experimental data by Brzek *et al.* (2008), a similar ratio δ/k must be specified. Thus, based on this consideration, it was decided to scale the original surface topography in all dimensions by a factor of 6 in order to achieve the same value of $\delta_{inl}/k = 71$ (or $k/\delta_{inl} = 0.014$) as in Brzek *et al.*

https://doi.org/10.1017/jfm.2013.326 Published online by Cambridge University Press

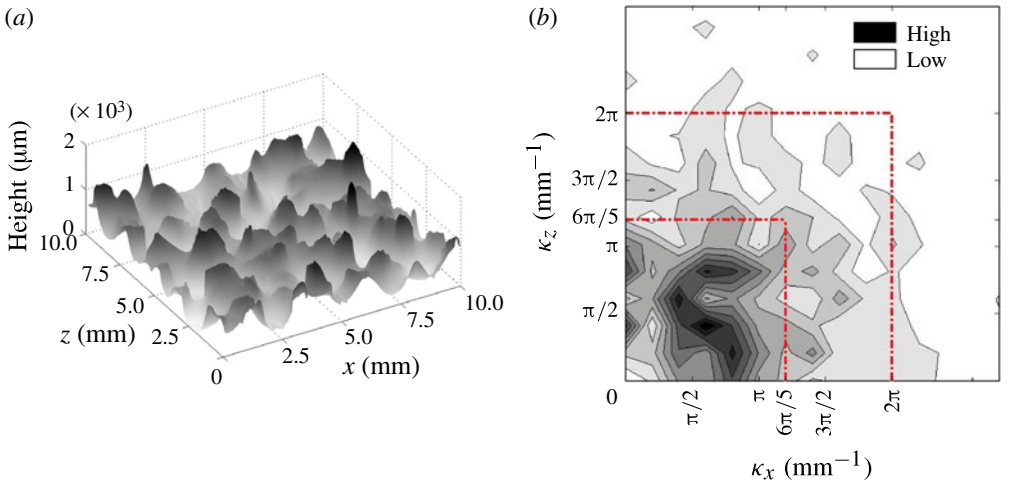


FIGURE 2. (Colour online) (*a*) Primitive data showing a sample unit of surface roughness topography and (*b*) fast Fourier transform of the sample unit.

(2008), which gives $k^+ \simeq 11$. Furthermore, the value of k^+ is computed by averaging the five highest peaks and five deepest valleys of the actual sandpaper topography and the same criterion is employed in the numerical procedure. Nonetheless, even after scaling, the primitive data are still interpolated onto a computational mesh and it is essential that the features which characterize the surface topography are not 'smeared' out. On the other hand, the use of 132×666 grid points per sample unit (now 60 mm) in our DNS would demand extraordinary CPU time. According to the current domain dimensions, approximately 50 by 8 'bricks' are needed in the streamwise and spanwise directions, respectively. This would require 6600×5328 points in the streamwise and spanwise directions in the computational domain to reach the same resolution as the laser device. Moreover, the consideration of $N_y = 150$ will give a total number of points equal to 5.3 billion, still difficult to solve with today's supercomputers in a reasonable time. This is where knowledge of the roughness spectra shown in figure 2 is critical. It must be ensured that wavelength resolution possessed by the simulation grid can resolve the most important wavelengths of the roughness topography. Therefore, the number of computational nodes required in a sample unit (now 60 mm) in one direction (say the x direction) to resolve up to a specific wavenumber, κ_{cuttof}, can be computed by the following equation:

$$2\pi \frac{n_x - 1}{2L_x} = \kappa_{cutoff}, \tag{3.3}$$

in which n_x is the number of nodes per scaled sample unit (60 mm), L_x is the length of the sampling unit in the x direction, and κ_{cutoff} is the maximum wavenumber in the x direction which can be resolved in the simulations. Recall that the FFT analysis reveals that wavenumbers less than 3.77 mm^{-1} for the unscaled sample contain most of the content of the spectrum. Thus, one can take 3.77 mm^{-1} as κ_{cutoff} for the original sample, which translates to 0.628 mm^{-1} for the scaled sample. Then, considering L_x is 60 mm, n_x is computed to be 13. The z direction has the same κ_{cutoff} for the scaled sample unit, so $n_z = 13$ as well. For the current study, the computational mesh contains 9 nodes per scaled sample unit (60 mm) in the streamwise direction, and 18 nodes

https://doi.org/10.1017/jfm.2013.326 Published online by Cambridge University Press

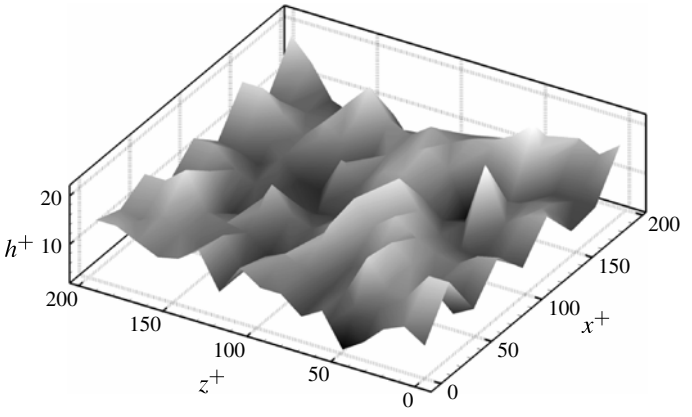


FIGURE 3. Actual roughness sample used in simulations labelled with inner units. The scaled physical size is 60 mm × 60 mm.

per scaled sample unit in the spanwise direction. Hence, the resolution of the current mesh in the streamwise direction may be marginally sufficient, but in the spanwise direction the mesh is more than sufficient. The actual scaled sample unit used in the simulations is shown in figure 3 in inner units. This sample unit can be used as a single 'brick' to cover the entire wall of the computational domain. The sample units or 'bricks' are mirrored an appropriate amount of times to fill the bottom of the computational box such that the interfaces between neighbouring sample units contain no discontinuities. Although the mesh resolution in the streamwise direction might not fully characterize the sand grit surface topography, it is demonstrated in appendix B (Kolmogorov's length and time scales) that the computational mesh is able to fully resolve the flow field. The FFT analysis also suggests that the roughness effects were mainly concentrated on the low-wavenumber (long-wavelength) range. In addition, the resolution of the laser measurements on the sample unit was over-abundant.

4. Case setup

The parameters used to set up the current DNS case are shown in table 3. Additionally, the parameters for the smooth DNS of Araya *et al.* (2009) and the experiment carried out by Brzek *et al.* (2008) are shown for comparison. First, it may be observed that inlet parameters for the present case and that of Araya *et al.* (2009) are very comparable. Next, notice that the parameters for the current DNS case match those of Brzek *et al.* (2008) reasonably well with some minor differences in Reynolds number, roughness parameter k^+ and inlet boundary layer thickness. However, the unitary free stream velocity U_∞ employed in simulations significantly differs from experiments.

In order to ensure that the flow becomes fully uncorrelated before flow recycling begins, the recycle plane is placed approximately 80 % ($L_x^+ \approx 7000$ dimensionless streamwise wall units) of the streamwise domain length downstream of the inlet in all cases. This ensures an almost-zero value for the two-point correlation (Araya *et al.* 2009) of any fluctuating flow parameter and allows the turbulent structures to evolve independently of the recycle location. In addition, the test plane is located approximately halfway between the inlet and recycle planes. In order to drive the turbulent flow through the initial transient period, the mean profile for the streamwise

https://doi.org/10.1017/jfm.2013.326 Published online by Cambridge University Press

Parameter	Present DNS	DNS, Araya *et al.* (2009)	Exp., Brzek *et al.* (2008)
Re_θ	2077–2439	1940–2300	2642–3109
δ^*/δ	0.175–0.178	0.147–0.150	0.188–0.193
H	1.5–1.51	1.36–1.37	1.47–1.5
k^+	11	0	15.16
u_τ (m s^{-1})	0.0475–0.046	0.043–0.042	0.469–0.424
δ^+_{inl}	1048	980	943
U_∞ (m s^{-1})	1	1	10

TABLE 3. Inlet parameters for the current DNS, the smooth surface DNS of Araya *et al.* (2009), and the rough surface experiments by Brzek *et al.* (2008).

velocity is fixed at the inlet. During the transient period, the wall-normal and spanwise components of the mean velocity, as well as all the fluctuations, are rescaled from the recycle plane. After the power law parameters reach a statistical steady state, the mean streamwise velocity profile also starts to be scaled from the recycle plane and smoothly re-injected at the inlet. By switching from the fixed to the recycled velocity profile, the transient period was shortened by approximately 10 000 time steps. The influence of the initial fixed velocity profile is removed very shortly after the recycling is turned on. The mean velocity profiles in this case were obtained from the theory of GC97 for zero pressure gradient flows.

The current DNS case was run for approximately 50 000 time steps (approximately 58 flow-through), with the time step size set to $\Delta t^+ \approx 0.535$ based on $(u_\tau)_{inl}$. The initial conditions were taken from a smooth surface DNS case which was run during $t^+ = 17\,000$. The statistics were taken in the last $t^+ = 6955$ non-dimensional time. Since the current rough surface DNS actually starts from the 63 000th time step of the smooth case, the time series in figure 4(*a,b*) and figure 5 are shown beginning at this time step. After the passage of 85 000 time steps (or $t^+ = 17\,000$), the power law parameters γ_θ and γ_δ reached a statistical steady state, which can be seen in figure 4(*a,b*). It can be observed from figure 4(*a*) that the inner power law exponent reaches a steady state value of approximately -0.932 while the outer power law exponent, shown in figure 4(*b*), reaches a value of approximately 0.738. The exponent γ_δ has already been implemented in Araya *et al.* (2011), where it was assumed that $\delta \sim x^{\gamma_\delta}$ or $\delta/x \sim Re_x^{\gamma_\delta - 1}$ in order to compute the scaling parameter $\mathrm{d}\delta/\mathrm{d}x$. This procedure of computing $\mathrm{d}\delta/\mathrm{d}x$ was observed to be more stable than getting the boundary layer growth rate by means of finite difference. Brzek *et al.* (2008, 2009) have reported an experimental value of $\gamma_\delta \approx 0.64$ for sandpaper roughness with $k^+ = 15.16$, which is very close to the computed value in the present investigation. Furthermore, White (1974) has proposed an empirical correlation in smooth ZPG flows for the boundary layer thickness as a function of the streamwise coordinate, which reads $\delta/x \sim Re_x^{-0.2}$. The value obtained for the present rough case was $\delta/x \sim Re_x^{0.738-1=-0.262}$, which indicates a more pronounced decrease of δ/x for rough walls in terms of the streamwise Re_x. The flow field for the current DNS has been spatially averaged in the spanwise direction, and time-averaged from the 84 000th to the 97 000th time steps (with 1300 flow realizations). The time variation of the friction velocity ratio at the inlet plane to the recycle plane is shown in figure 5.

https://doi.org/10.1017/jfm.2013.326 Published online by Cambridge University Press

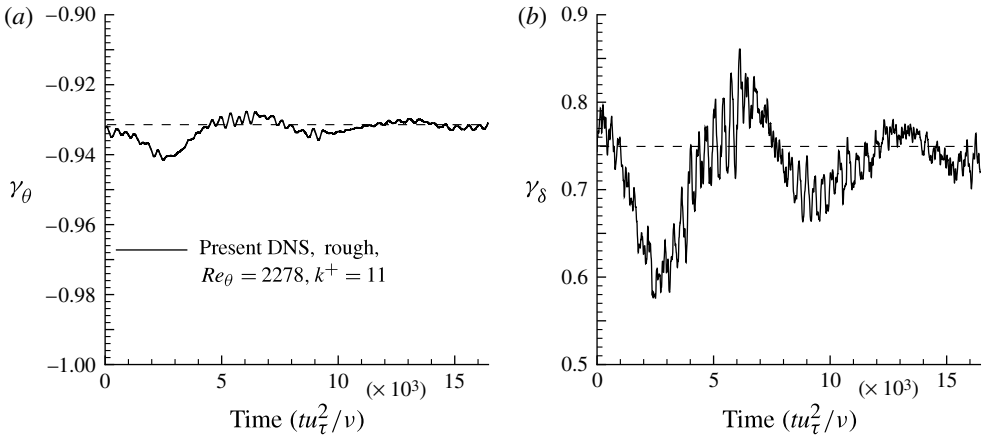


FIGURE 4. Time series of the dynamically computed power law exponents for the current DNS: (*a*) the inner scale, friction velocities, and (*b*) the outer scale, boundary layer thickness.

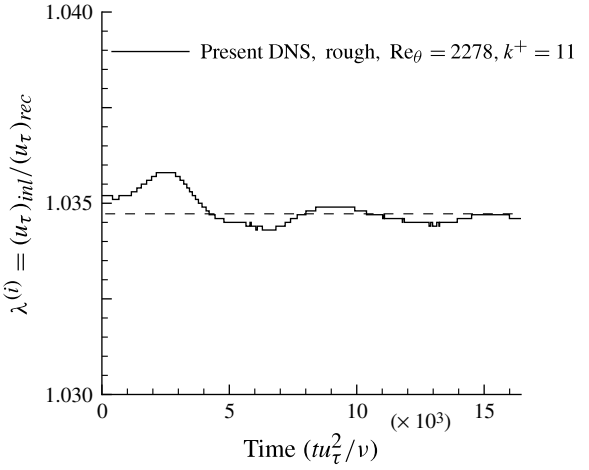


FIGURE 5. Time series of λ_{inner}, the ratio of the friction velocities at the inlet to the recycle plane.

Notice that the λ_{inner} factor, which is used directly as the scale for the inner boundary layer, does not fluctuate as much as the power law parameters because of cancellations that occur through variations of other parameters (Araya *et al.* 2011). Moreover, from the time series in figure 5, one can observe values close to $\lambda_{inner} \approx 1.035$. Brzek *et al.* (2008, 2009) reported an experimental exponent of -0.36 for $k^+ = 15.16$, e.g. $\theta/x \approx Re_x^{\gamma_\theta=-0.36}$. This exponent significantly differs from the value obtained in the present simulations (≈ -0.932). This discrepancy might be attributed to the different free stream velocity, $U_\infty = 10$ m s^{-1}, employed in experiments against the unitary value considered in simulations, based on previous studies by Castillo & Johansson (2002). However, it seems that the scaling parameter λ_{inner} is not very sensitive to the power γ_θ. The power $\gamma_\theta = -0.36$ would have produced a value of λ_{inner} barely 5 % lower than those computed in the present DNS.

https://doi.org/10.1017/jfm.2013.326 Published online by Cambridge University Press

5. Numerical results

5.1. *Flow parameters*

Rough surfaces cause difficulties when computing the wall shear stress as the roughness elements disturb the viscous sublayer of the boundary layer, and in some cases, destroy it completely (Brzek *et al.* 2008; Cal *et al.* 2009). As a result, direct measurements of the velocity gradient at the wall no longer provide a measurement of the wall shear stress as in the smooth case. In order to solve the problem, Schultz & Flack (2003) employed a modified form of the Clauser chart from which u_τ is obtained from mean velocity data by fitting a log law. This approach is based on the validity of the classical law of the wall for turbulent boundary layers, and in many cases, it is extended to low Reynolds numbers where an inertial subrange does not exist (GC97), but it is mainly a meso-layer. Using this technique in the presence of surface roughness requires the specification of additional parameters (Brzek *et al.* 2008). Because of these difficulties, the constant stress layer (5.1) is employed here to calculate the wall shear stress for the current DNS:

$$\frac{\tau_w}{\rho} = \nu \frac{\partial U}{\partial y} - \langle uv \rangle. \tag{5.1}$$

Equation (5.1) is used during the postprocessing stage, after the sample for statistics computation has been collected. Equation (5.1) is applied along the streamwise direction to compute the local skin friction coefficient, C_f, and it requires the mean streamwise velocity and Reynolds shear stress profiles (spanwise averaged) in the wall-normal direction at every x location. Furthermore, at every x station, the velocity derivatives, $\partial U/\partial y$, were computed by a central difference at five different vertical points: two below and two above the location of $\langle uv \rangle_{max}$. This zone is called the constant stress layer. The corresponding velocity derivatives and Reynolds shear stresses were then averaged in order to obtain the local wall stress, τ_w. Finally, the local skin friction coefficient is computed by means of (5.2). It is worth clarifying that using the constant stress layer equation (5.1) produces more accurate values for the skin friction coefficient than using the momentum integral equation (2.7), but it requires knowledge of $\langle uv \rangle$. The 'online' calculation of the cross-correlation $\langle uv \rangle$ is feasible; however, it demands several time steps for convergence. For that reason, the momentum integral equation has been employed to compute λ_{inner} dynamically, which only involves knowledge of the mean streamwise velocity with a faster rate of convergence. This makes the momentum integral equation very appropriate for 'online' use. Furthermore, because the dynamic multi-scale approach only needs the ratio of friction velocities at the inlet and recycle planes, not the actual values of u_τ, this seems to produce an error compensation. Moreover, the computed value of λ_{inner} by means of the constant stress layer equation was approximately 2 % different from that obtained by the momentum integral equation.

The skin friction coefficient and the friction velocity can be computed from the wall shear stress using the relationship

$$\frac{C_f}{2} = \frac{\tau_w}{\rho U_\infty^2} = \frac{u_\tau^2}{U_\infty^2}. \tag{5.2}$$

The skin friction coefficient for the present DNS case is plotted in figure 6 as a function of the Reynolds number. In addition, the skin friction coefficient for the smooth DNS case of Araya *et al.* (2009) and for the experiments carried out by Brzek *et al.* (2008) and Schultz & Flack (2003) are shown on the same axes for comparison.

https://doi.org/10.1017/jfm.2013.326 Published online by Cambridge University Press

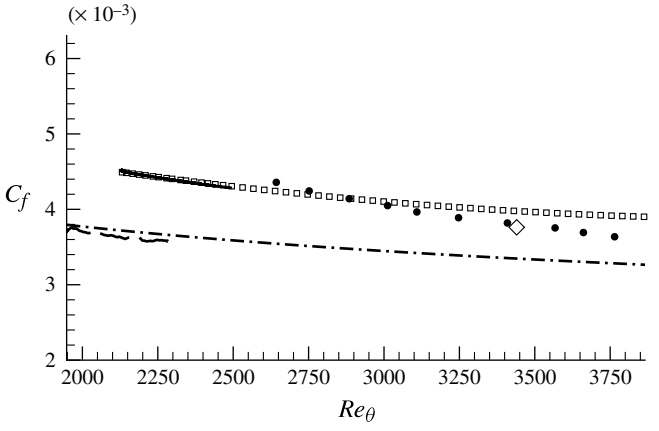


FIGURE 6. Skin friction coefficient: ———, present DNS, rough, $Re_\theta = 2077$–2439, $k^+ = 11$; — — —, Araya *et al.* (2009), DNS, smooth, $Re_\theta = 1940$–2300; •, Brzek *et al.* (2008), experiment, rough, $Re_\theta = 2600$–3900, $k^+ = 15.16$; ◇, Schultz & Flack (2003), experiment, rough, $Re_\theta = 3440$, $k^+ = 9$; — · — · —, George & Castillo (1997), theory, smooth; □, Brzek *et al.* (2009), theory, rough.

It is observed that the current DNS follows a similar trend to the data of Brzek *et al.* (2008) and Schultz & Flack (2003). The theoretical evaluation of the skin friction based on the theory presented by Brzek *et al.* (2009) is shown on the same plot using the input parameters from the current rough surface DNS. One can observe a very close match between the theoretical and numerical evaluation of the skin friction coefficient. The percentage difference between the theory of Brzek *et al.* (2009) and the current DNS is less than 1 %.

The shape factor as a function of the streamwise coordinate for the current DNS, the smooth DNS of Araya *et al.* (2009), the laser Doppler anemometry (LDA) measurements of Brzek *et al.* (2008), the LDA measurements of Castillo & Johansson (2002), the smooth surface DNS of Khujadze & Oberlack (2004), and the theory of GC97 are shown in figure 7(*a*). Note that due to different ranges of Re_θ, it is not possible to calculate percentage errors between the present DNS and the experiments of Brzek *et al.* (2008). The expected behaviour is observed; both the displacement thickness and the momentum thickness are augmented by the presence of the surface roughness, but the roughness has a stronger effect on the displacement thickness, resulting in an overall increase of the shape factor observed for the current DNS from the results of Araya *et al.* (2009), GC97, Castillo & Johansson (2002) and Khujadze & Oberlack (2004) by 11, 10, 8 and 11 % respectively. In figure 7(*b*), the non-dimensionalized momentum thickness is plotted as a function of the streamwise coordinate for the current DNS, the smooth DNS of Araya *et al.* (2009), and the LDA measurements of Brzek *et al.* (2008). Excellent agreement exists between the DNS and LDA experiments. One can observe that as the level of surface roughness is increased, the momentum thickness shifts downward and to the right. However, a higher inlet momentum thickness was used for cases with surface roughness, resulting in lower values of the momentum thickness ratio θ/θ_{inlet}, as seen in figure 7(*b*). Similarly, the ratio δ/δ_{inlet} is depicted by figure 7(*c*), in good agreement with experimental data by Brzek *et al.* (2008). Note the almost linear trends of $\delta(x)$ for the smooth and rough walls. In addition, notice the presence of a short developing section in δ at the inlet

https://doi.org/10.1017/jfm.2013.326 Published online by Cambridge University Press

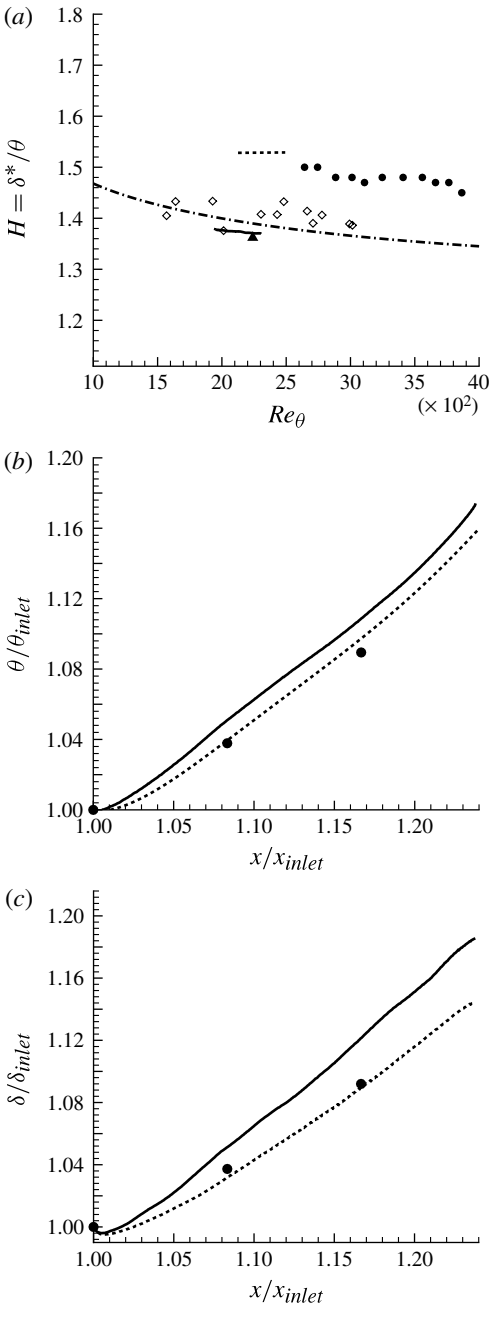


FIGURE 7. (*a*) Shape factor distribution: ------, present DNS, rough, $Re_\theta = 2077$–2439, $k^+ = 11$; ———, Araya *et al.* (2009), DNS, smooth, $Re_\theta = 1940$–2300; ●, Brzek *et al.* (2008), experiment, rough, $Re_\theta = 2600$–3900, $k^+ = 15.16$; — · — · —, George & Castillo (1997), theory, smooth; ◇, Castillo & Johansson (2002), experiment, smooth; ▲, Khujadze & Oberlack (2004), DNS, smooth, $Re_\theta = 2240$. (*b*) Momentum thickness distribution: ------, present DNS, rough, $Re_\theta = 2077$–2439, $k^+ = 11$; ———, Araya *et al.* (2009), DNS, smooth, $Re_\theta = 1940$–2300; ●, Brzek *et al.* (2008), experiment, rough, $Re_\theta = 2600$–3900. (*c*) Boundary layer thickness distribution: lines as in (*b*).

https://doi.org/10.1017/jfm.2013.326 Published online by Cambridge University Press

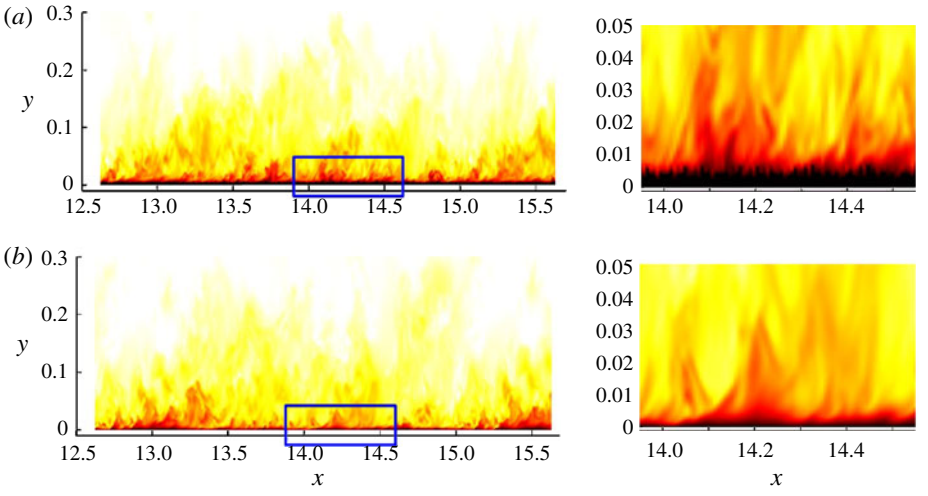


FIGURE 8. (Colour online) Iso-contours of the instantaneous streamwise flow field for the (*a*) rough wall and (*b*) smooth wall DNS cases. Close-ups of the boxed areas are shown on the right.

region for the smooth and rough DNS cases, where the flow parameters behave in a non-physical sense (decreasing δ). However, this developing region has been noted to be very short, of the order of $1\delta_{inlet}$.

5.2. *Velocity field*

Figure 8 shows the iso-contours of the instantaneous streamwise velocity for the present rough surface DNS and the smooth DNS of Araya *et al.* (2009). The streamwise slice was taken through the centre of the computational domain. Qualitative comparison of the instantaneous flow field allows us to deduce that the surface roughness increases the overall thickness of the boundary layer, in addition to enhancing the near-wall mixing and homogeneity in the structures within the boundary layer. This idea will be revisited in § 6. It can also be observed that the proposed dynamic method does not induce periodicity in the flow as stated by Simens *et al.* (2009).

The mean velocity profiles for the current rough wall DNS and the smooth wall DNS of Araya *et al.* (2009) are plotted using a deficit scaling and inner units, as shown in the inset, at a Reynolds number of $Re_\theta \approx 2278$ in figure 9, using a semi-log scale. For a qualitative comparison, the experimental data of Schultz & Flack (2003) and Brzek *et al.* (2008) are also plotted on the same axes. The current DNS results lie close to the roughness experiments carried out by Schultz & Flack (2003) and Brzek *et al.* (2008), which may be due to the closeness in the roughness parameter k^+. In comparing the smooth wall DNS with the rough wall DNS, it is evident that the surface roughness causes a downward shift in the entire mean velocity profiles, a consequence of the increased velocity deficit due to the presence of the surface roughness. This outcome is consistent with the literature, which indicates that as the roughness height is increased, the roughness protrudes further into the boundary layer, causing a deceleration of the velocity field. One can quantitatively compare the rough and smooth DNS cases in figure 9 and determine that this type of roughness causes a maximum velocity deficit of approximately 4 %. Again, the experimental data of

https://doi.org/10.1017/jfm.2013.326 Published online by Cambridge University Press

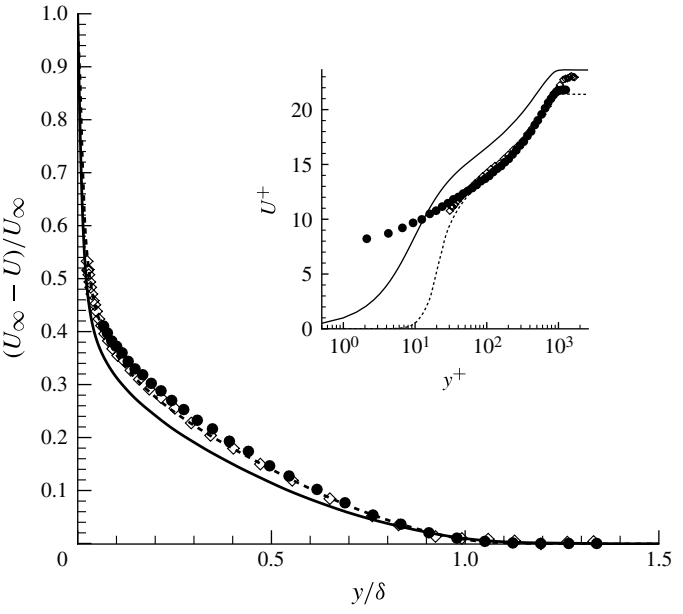


FIGURE 9. Mean velocity profiles using outer deficit scaling (main) and inner units (inset): ------, present DNS, rough, $Re_\theta = 2278$, $k^+ = 11$; ———, Araya *et al.* (2009), DNS, smooth, $Re_\theta = 2239$; •, Brzek *et al.* (2008), experiment, rough, $Re_\theta = 2642$, $k^+ = 15.16$; ◇, Schultz & Flack (2003), experiment, rough, $Re_\theta = 3440$, $k_s^+ = 9$.

Schultz & Flack (2003) and Brzek *et al.* (2008) are plotted on the same axes, and similar behaviour to that of figure 9 is observed. Furthermore, one can clearly see the shift in the mean velocity profiles in wall units (inset) for the rough data. Good agreement is observed between the present DNS rough case and the experimental data of Schultz & Flack (2003) and Brzek *et al.* (2008), with some discrepancies in the wake attributed to differences in Reynolds number.

The streamwise component of the Reynolds normal stress, $\langle u'^2 \rangle$, for the smooth and rough DNS cases, in addition to the experimental measurements of Brzek *et al.* (2008) and Schultz & Flack (2003), is presented in figure 10 using outer and inner scaling. The vertical line in the inset represents the local minimum roughness height. The results of the present DNS demonstrate that at the Reynolds numbers considered here, the current surface roughness slightly raises the peak of the streamwise component when using outer scaling (i.e. U_∞). However, roughness reduces the peak of $\langle u'^2 \rangle$ when considering inner scaling (i.e. u_τ). This is because U_∞ remains constant in both cases, but the skin friction coefficient and u_τ increase due to the presence of roughness, as seen in figure 6. Below the roughness peak (inside the roughness element), the streamwise component quickly decays to zero. The inset of figure 10 shows an obvious shift in inner units and semi-log scale. The decrease in peaks of $\langle u'^2 \rangle$ for the rough case is consistent with many earlier experiments and the DNS results of Scotti (2007). In experiments the proposed theory for this reduction is that surface roughness elements break up the streamwise vortical structures near the wall.

Moreover, slight scattering can be observed in figure 10(*a*) for the experiments, particularly in the data of Brzek *et al.* (2008), at values of $y/\delta < 0.15$, due to limitations in spatial resolution of the experiments and inability to accurately

https://doi.org/10.1017/jfm.2013.326 Published online by Cambridge University Press

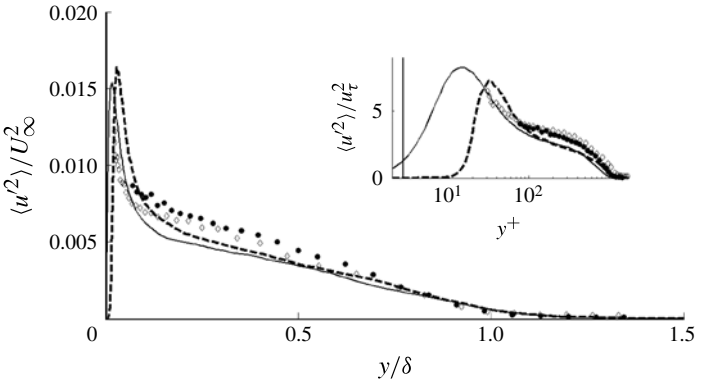


FIGURE 10. Streamwise component of the Reynolds normal stresses in outer units (main) and inner units (inset): ------, present DNS, rough, $Re_\theta = 2278$, $k^+ = 11$; ———, Araya *et al.* (2009), DNS, smooth, $Re_\theta = 2239$; •, Brzek *et al.* (2008), experiment, rough, $Re_\theta = 2642$, $k^+ = 15.16$; ⋄, Schultz & Flack (2003), experiment, rough, $Re_\theta = 3440$, $k^+ = 9$.

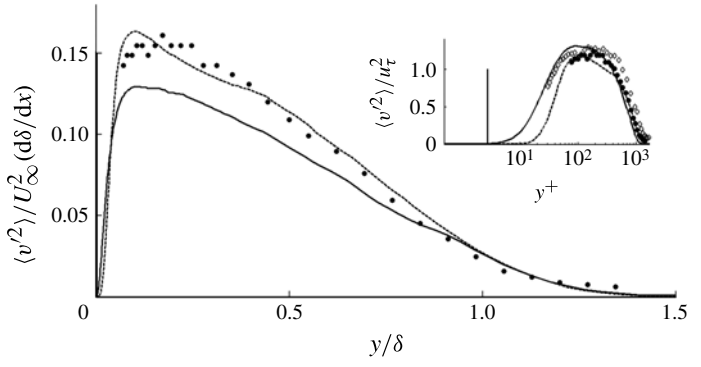


FIGURE 11. Wall-normal component of the Reynolds stresses in outer units (main) and inner units (inset). Lines and symbols as in figure 10.

determine the true shift in origin (the same holds for the wall-normal and Reynolds shear components). Also, it may be observed in figure 10 that for $y/\delta \in [0.1, 0.6]$, there is less agreement between the experimental and DNS data. This could be due to: (i) the Reynolds number not being high enough; (ii) low mesh resolution in the streamwise direction. Moreover, the Kolmogorov length scale computation (see appendix B) has indicated that the Δy^+ distribution is able to represent the flow details accurately. However, the streamwise resolution Δx^+ is not able to reproduce all the details on the surface roughness. In addition, we have performed statistical computations using 2700 flow realizations and obtained virtually identical results to those done using 1300 flow realizations. For this reason, it is believed that 1300 is a sufficient number of realizations.

The wall-normal component of the Reynolds normal stress, $\langle v'^2\rangle$, is plotted in figure 11 using outer and inner scaling. The most significant differences for $\langle v'^2\rangle$ profiles between the smooth and rough DNS cases are observed in peak values, which increase due to roughness for the $U_\infty^2 \mathrm{d}\delta/\mathrm{d}x$ scaling, but the opposite occurs for the

https://doi.org/10.1017/jfm.2013.326 Published online by Cambridge University Press

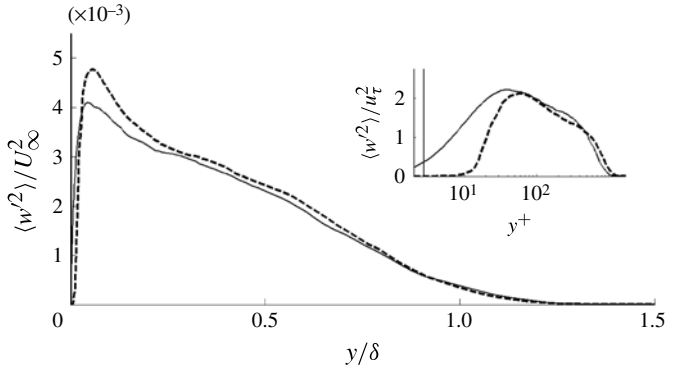


FIGURE 12. Spanwise component of the Reynolds normal stresses in outer units (main) and inner units (inset). Lines as in figure 10.

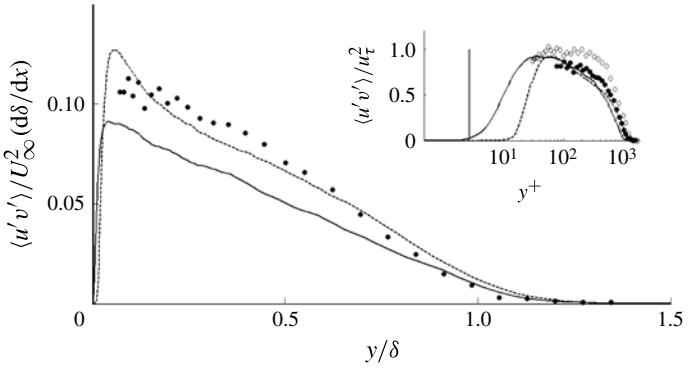


FIGURE 13. Reynolds shear stresses in outer units (main) and inner units (inset). Lines and symbols as in figure 10.

u_τ^2 scaling. Furthermore, much better agreement of the present DNS rough data with experiments by Brzek *et al.* (2008) can be observed in figure 11.

The spanwise component of the Reynolds normal stress, $\langle w'^2\rangle$ is plotted in figure 12 using outer and inner scaling. Experimental data for this velocity component was not available for comparison since only two components of the velocity were measured. As in the other components of the Reynolds stresses, increases or decreases of peak values due to the presence of roughness are observed according to the scale used, i.e. U_∞^2 or u_τ^2, respectively. In addition, the smooth and rough profiles almost collapse for $y/\delta > 0.5$ when considering outer units. However, some differences are observed for $y^+ > 200$ in inner units.

Furthermore, the Reynolds shear stresses, $\langle u'v'\rangle$, are plotted in figure 13 using outer and inner scaling. Higher peak values of the Reynolds shear stress are observed in the $U_\infty^2\mathrm{d}\delta/\mathrm{d}x$ scaling due to roughness. However, these peaks are very similar in the present rough and smooth cases when using inner units. Again, significant differences are observed in the outer layer where the Reynolds shear stress for the rough wall has a stronger presence than the smooth case. The experimental data of Schultz & Flack (2003) appear to suffer from spatial resolution limitations in the Reynolds shear

https://doi.org/10.1017/jfm.2013.326 Published online by Cambridge University Press

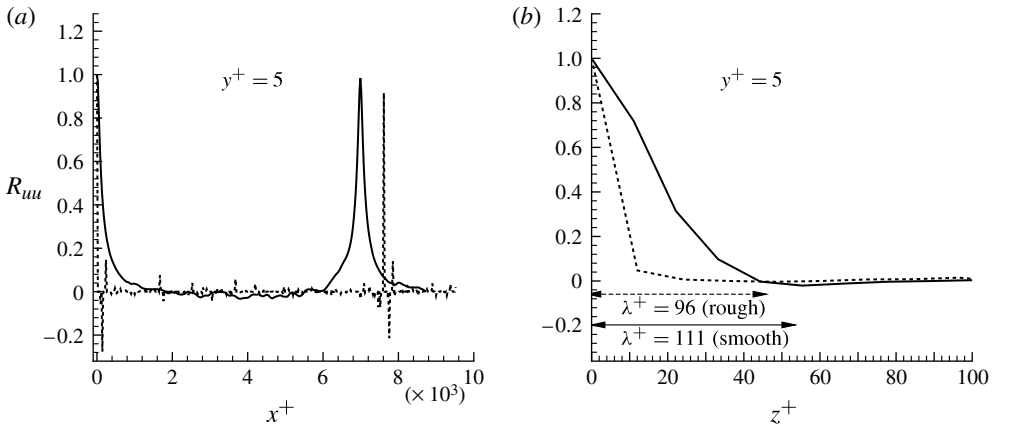


FIGURE 14. Two-point correlations R_{uu} for the smooth and rough cases as functions of (*a*) x^+ and (*b*) z^+ at a wall-normal height of $y^+ = 5$: ------, present DNS, rough, $k^+ = 11$; ———, Araya *et al.* (2009), DNS, smooth.

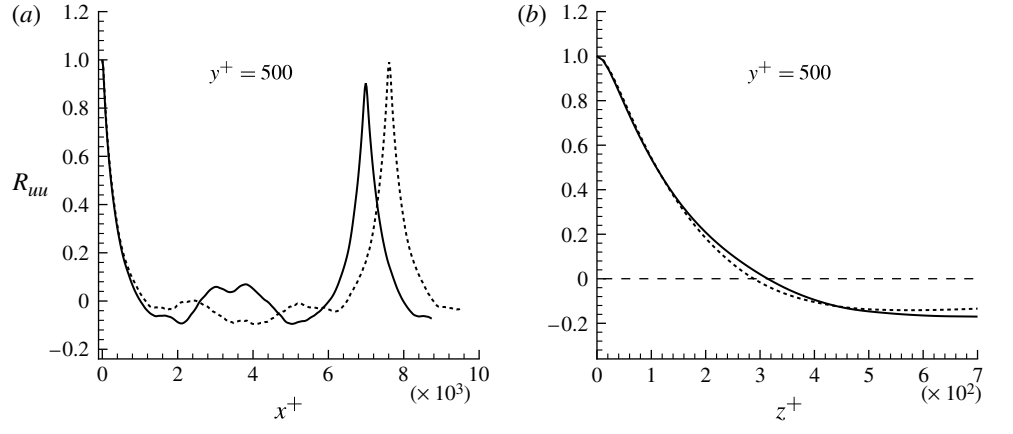


FIGURE 15. Two-point correlations R_{uu} for the smooth and rough cases as functions of (*a*) x^+ and (*b*) z^+ at a wall-normal height of $y^+ = 500$. Lines as in figure 14.

component, especially in the near-wall region, and better agreement with experimental data by Brzek *et al.* (2008) can be observed.

5.3. *Two-point Correlations*

Figures 14 and 15 plot the two-point correlation of the streamwise velocity fluctuations as functions of x^+ and z^+ at wall-normal heights of $y^+ = 5$ (inner region) and $y^+ = 500$ (outer region). The two-point correlation with dependence on x and y is defined in the usual way as

$$R_{uu}(x; y) = \frac{\langle u'(0, y, z, t)u'(x, y, z, t)\rangle}{u'_{rms}(0, y)u'_{rms}(x, y)}, \tag{5.3}$$

where averaging is performed over t and z. The two-point correlation with dependence on z is computed similarly.

https://doi.org/10.1017/jfm.2013.326 Published online by Cambridge University Press

We can observe from 14(*a*) and 15(*a*) the existence of a strong correlation at the recycle plane, also reported by Stolz & Adams (2003), which is due to the rescaling and recycling method. For both the smooth and rough cases at both wall-normal locations, the correlation decays rapidly to zero away from the inlet plane. It may also be observed that, in general, the largest differences between the correlations for the smooth and rough cases occur at $y^+ = 5$, since this is in the inner region and more specifically inside the roughness sublayer.

Figure 14(*b*) depicts R_{uu} profiles along the spanwise direction, and locations of z^+ at which a local minimum exists are labelled. These local minima indicate an average spacing ($\lambda^+ = \lambda u_\tau/\nu$) of 111 for smooth and 96 for rough. This is within the generally accepted spacing (100 ± 20) for near-wall streaks (Moin & Moser 1989; Kim & Moser 1987). Thus, the spacing of the streaks is slightly less in the rough case than in the smooth case. It may also be observed from figure 14(*a,b*) that streamwise velocity fluctuations in the rough case become uncorrelated much more quickly in both the streamwise and spanwise directions than in the smooth case. In the spanwise direction, the rough case correlation drops almost to zero by $z^+ \approx 10$, whereas for the smooth case a comparable value does not occur until $z^+ \approx 45$. In the streamwise direction, the rough case fluctuation exhibits almost no correlation. This is primarily due to the fact that the no-slip condition was displaced to the top of the roughness heights. That is, at this value of y^+, $\langle u'^2 \rangle$ is either identically 0 or very close to it.

For the correlations computed at $y^+ = 500$ (the outer region) only the half-domain is shown, because of the symmetry induced by periodic boundary conditions. There is much less difference observed between the smooth and rough cases. In the spanwise direction, the correlations are almost identical, the only discernible difference being that, for the rough case, the correlation is slightly lower in the centre and slightly higher at the edge. In the streamwise direction, comparable behaviour between the correlations is observed, though it may be noted that the rough case appears to be slightly less correlated than the smooth case.

Furthermore, two-point correlations for the wall-normal and spanwise velocity fluctuations in the streamwise and spanwise directions are depicted by figures 16 and 17 at $y^+ = 5$ and 500, respectively. Profiles similar to those obtained by Stolz & Adams (2003) can be observed. It is seen that wall-normal and spanwise velocity fluctuations are decorrelated by a quarter-domain length in the spanwise direction (at most, in the outer layer, i.e. at $y^+ = 500$) and around $x^+ \approx 400$ in the streamwise direction. This confirms that the computational domain and the recycle plane location are sufficiently large.

6. POD analysis

POD is performed on the velocity fluctuations, $\boldsymbol{u}(\boldsymbol{x}, t)$, of the DNS simulation. There are three major reasons for performing this analysis: (i) to gain another validation of the dynamic multi-scale approach by comparing the dominant POD mode computed using the current DNS with simulations performed using more computationally demanding methods; (ii) to further increase our knowledge of how flow structure varies between the smooth and rough cases; and (iii) to support the notion that roughness may affect large scales of the flow across the boundary layer, particularly when $k/\delta < 1/50$ and Re_θ is below 10 000 (non-existence of a true overlap).

The goal of performing a POD analysis is to expand the fluctuating velocity field in terms of a finite number of spatially dependent modes and time-dependent coefficients: $\boldsymbol{u}(\boldsymbol{x}, t) = \sum_{n=1}^{N} a_n(t)\, \boldsymbol{\Phi}(\boldsymbol{x})$. Detailed derivation of the POD is presented in many studies,

https://doi.org/10.1017/jfm.2013.326 Published online by Cambridge University Press

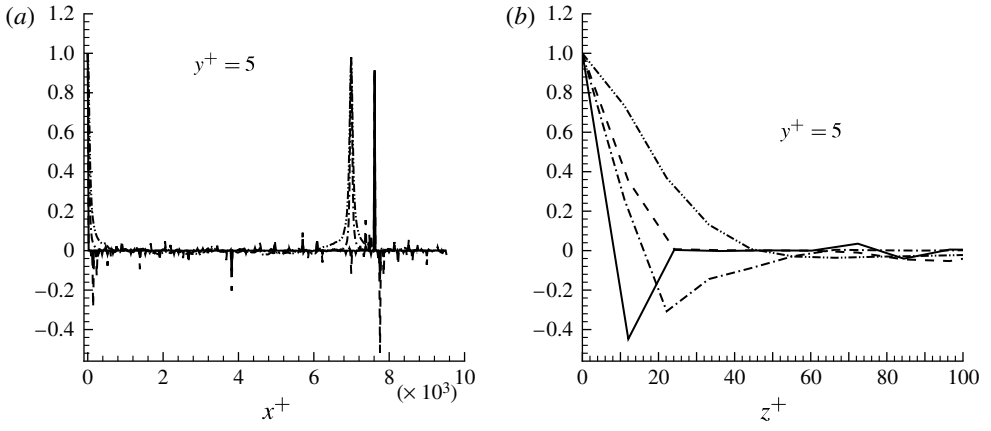


FIGURE 16. Two-point correlations R_{vv} and R_{ww} for the smooth and rough cases as functions of (*a*) x^+ and (*b*) z^+ at a wall-normal height of $y^+ = 5$: ———, R_{vv}, rough; - - - - - -, R_{ww}, rough; — - — -, R_{vv}, smooth; — - - — - - — - -, R_{ww}, smooth.

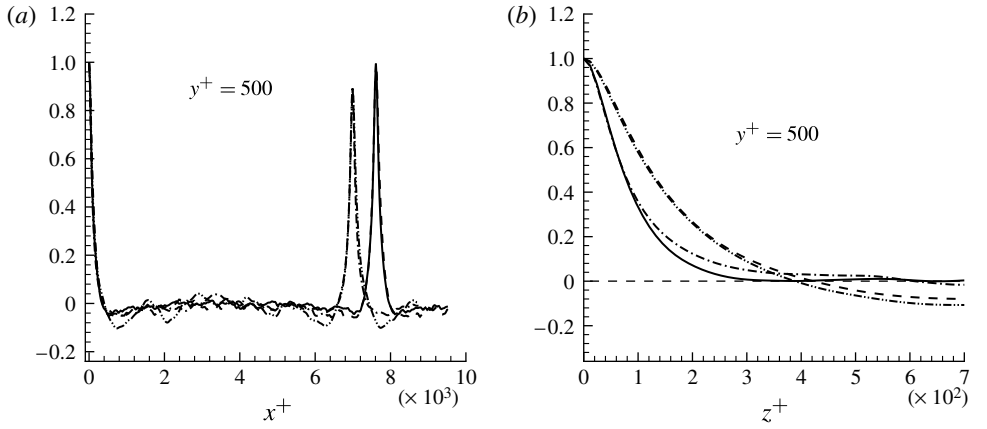


FIGURE 17. Two-point correlations R_{vv} and R_{ww} for the smooth and rough cases as functions of (*a*) x^+ and (*b*) z^+ at a wall-normal height of $y^+ = 500$. Lines as in figure 16.

such as Holmes, Lumley & Berkooz (1997). The standard integral equation associated with the POD analysis is given by

$$\int_D \boldsymbol{R}(\boldsymbol{x}, \boldsymbol{x}')\, \boldsymbol{\Phi}(\boldsymbol{x}')\mathrm{d}x' = \lambda\, \boldsymbol{\Phi}(\boldsymbol{x}), \tag{6.1}$$

where $\boldsymbol{R}(\boldsymbol{x}, \boldsymbol{x}') = \langle \boldsymbol{u}(\boldsymbol{x}, t) \otimes \boldsymbol{u}^*(\boldsymbol{x}', t) \rangle$ is the two-point spatial correlation tensor, and λ and $\boldsymbol{\Phi}$ are the eigenvalues and eigenvectors, respectively, of the integral equation (equation (6.1)). The boundary layer is homogeneous and periodic in the spanwise (z) direction. Holmes *et al.* (1997) show that for these conditions, the POD modes in the spanwise direction are actually Fourier modes, so we can express the fluctuating

https://doi.org/10.1017/jfm.2013.326 Published online by Cambridge University Press

velocity field u_i' as

$$u_i(\boldsymbol{x}, t) = \sum_{k_z=-(N_z-1)/2}^{(N_z-1)/2} \hat{u}_i^{(k_z)}(x, y, t)\mathrm{e}^{2\pi\mathrm{i}(k_z z/L_z)}. \tag{6.2}$$

A POD is actually performed on the Fourier coefficients, that is, each $\hat{u}_i^{(k_z)}(x, y, t)$ is expanded as

$$\hat{u}_i^{k_z}(x, y, t) = \sum_{n=1}^{N} \hat{a}^{(k_z,n)}\hat{\phi}_i^{(k_z,n)}(x, y). \tag{6.3}$$

It is typical in DNS simulations for the number of grid points to be significantly higher than the number of uncorrelated realizations, so the method of snapshots by Sirovich (1987) is used to convert the eigenvalue problem from one involving the spatial correlation to one involving the time correlation. Therefore, the POD modes are expressed as linear combinations of the Fourier coefficients at each of the time steps used in the analysis $\hat{\phi}_i^{(k_z,n)}(x, y) = \sum_{j=1}^{N_t} c^{(k_z,n,t_j)}\hat{u}_i^{(k_z)}(x, y, t_j)$, which changes the eigenvalue problem (6.1) into one for the coefficients $\boldsymbol{c}^{(k_z,t_j)}$:

$$\sum_{j=1}^{N_t} M_{hj}^{(k_z)} c_j^{(k_z)} = \lambda^{(k_z)} c_h^{(k_z)}. \tag{6.4}$$

Notice that $M_{hj}^{(k_z)}$ is the time correlation matrix between Fourier coefficients of the same wavenumber at different snapshots:

$$M_{hj}^{(k_z)} = (\hat{\boldsymbol{u}}^{(k_z)}(x, y, t_j), \hat{\boldsymbol{u}}^{(k_z)}(x, y, t_h)). \tag{6.5}$$

The integration for calculating the inner products for M_{hj} is approximated using the trapezoidal rule, which was shown to be adequate for these calculations by Moin & Moser (1989). The calculated orthogonal POD modes are then normalized and the time-dependent coefficients may be found as

$$\hat{a}^{(k_z,n)} = (\hat{\boldsymbol{u}}^{(k_z)}(x, y, t), \hat{\boldsymbol{\Phi}}^{(k_z,n)}(x, y)). \tag{6.6}$$

Since the velocity fluctuations are real values, we have $\hat{\phi}_i^{(k_z,n)}(x, y) = \hat{\phi}_i^{*(-k_z,n)}(x, y)$, thus only modes for positive wavenumbers are required for the calculation. Mode indices n are numbered by decreasing eigenvalue: $n = 1$ for each wavenumber contributes the most to the kinetic energy contained in that wavenumber. For this POD analysis, a total of $N_t = 39$ uncorrelated snapshots were used, separated by a dimensionless time of $t^+ = 50$. Improved convergence of POD could, of course, be achieved by including additional time steps, but it was found that there was not very much change in the modes when more than 39 snapshots were used. To extract the fluctuations from the DNS data, both time and spatial averaging in the z direction were used to compute the mean velocities. Once the POD modes are known, a single time step of the fluctuating velocity field can be reconstructed as follows:

$$u_i(\boldsymbol{x}, \bar{t}) = \sum_{k_z=-(N_z-1)/2}^{(N_z-1)/2} \sum_{n=1}^{N} \hat{a}^{(k_z,n)}(\bar{t})\hat{\phi}_i^{(k_z,n)}(x, y)\mathrm{e}^{-2\pi\mathrm{i}(k_z z/L_z)}. \tag{6.7}$$

We denote $\phi_i^{(k_z,n)}(\boldsymbol{x}) = \hat{\phi}_i^{(k_z,n)}(x, y)\mathrm{e}^{-2\pi\mathrm{i}(k_z z/L_z)}$. Visualization and interpretation of the POD modes was discussed by Liu, Adrian & Hanratty (2001), and the present results

https://doi.org/10.1017/jfm.2013.326 Published online by Cambridge University Press

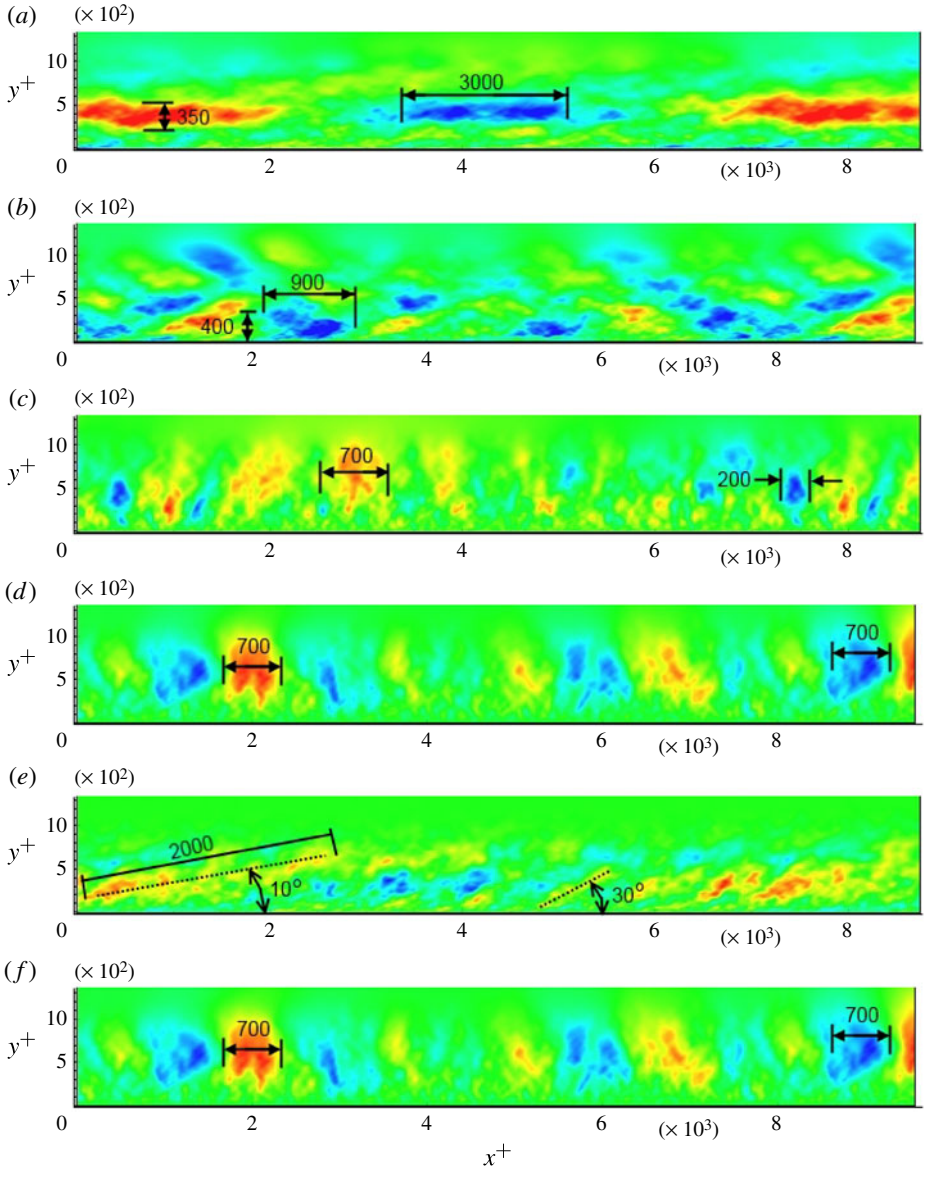


FIGURE 18. Velocity contours of the $n = 1$ smooth and rough modes of $k_z = 0$: (*a*) streamwise smooth, (*b*) streamwise rough, (*c*) wall-normal smooth, (*d*) wall-normal rough, (*e*) spanwise smooth, and (*f*) spanwise rough.

can be analysed similarly. They showed that $\mathrm{Im}[\phi_i^{(k_z,n)}] = \mathrm{Re}[\phi_i^{(k_z,n)}]$ after a $\pi/2$ phase shift, corresponding to a physical shift of $L_z/4k_z$. Thus, the velocity fluctuations are linear combinations of the real parts of the ϕ' with and without the shift.

Streamwise, wall-normal and spanwise velocity contours for $k_z = 0, n = 1$ for the smooth and rough cases are shown in figure 18 in inner units so that the outer region ($y^+ > 50$) can be clearly identified. Clearly shown in figure 18 are alternating high-speed/low-speed regions. This is very similar to the sinusoidal modes that would be

https://doi.org/10.1017/jfm.2013.326 Published online by Cambridge University Press

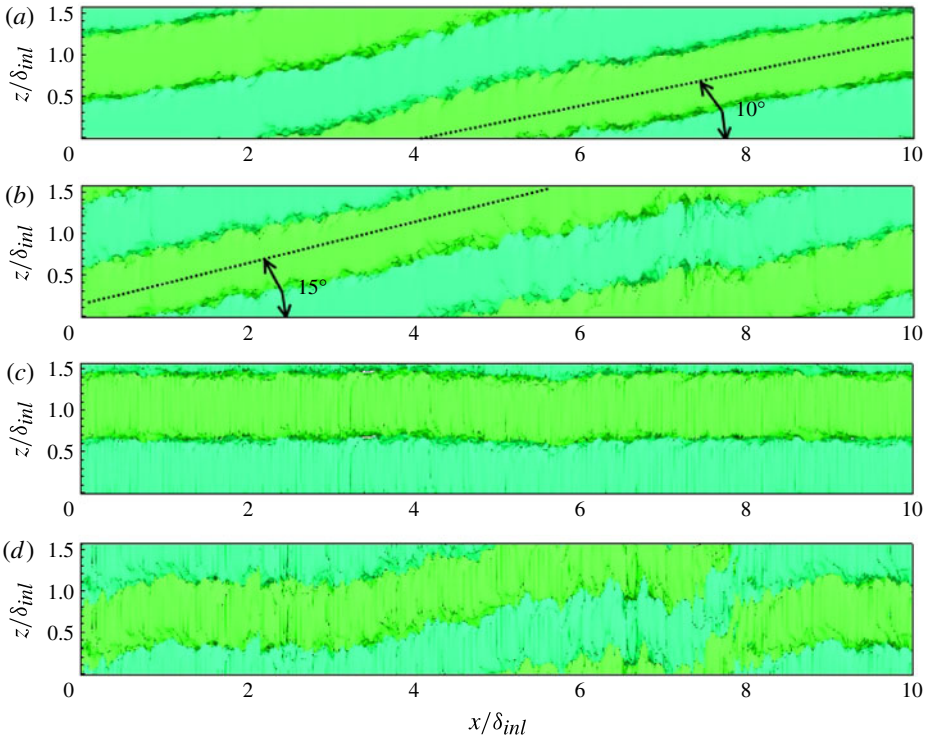


FIGURE 19. Iso-contours of fluctuating streamwise velocity u' for (*a*) $k_z = 1$, $n = 1$, (*b*) $k_z = 1$, $n = 2$ smooth, (*c*) $k_z = 1$, $n = 1$ rough, (*d*) $k_z = 1$, $n = 2$ rough.

present if flow was homogeneous, e.g. a channel (Baltzer, Adrian & Wu 2010). This flow pattern is also consistent with modes for travelling waves as discussed by Aubry, Guyonnet & Lima (1992). Virtually identical behaviour was presented by Baltzer *et al.* (2010), analysing the DNS simulation of a smooth ZPG turbulent boundary layer of Wu & Moin (2010). Iso-contours of streamwise velocity fluctuations are shown in figure 19. Comparative behaviour between the current DNS and that of Wu & Moin (2010) was also observed in the iso-contours of streamwise fluctuating velocity, as shown in figure 19. It can be observed that the iso-surfaces of streamwise velocity in the smooth case have a drift in the spanwise direction. This is thought to be a result of the dimension of the computational domain in that direction. If the domain is too thin, it is possible that spanwise forces will not average out, thus causing the drift observed here. Achieving very similar results for the most energetic POD modes is again very encouraging for the use of the dynamic multi-scale approach. We can also make some cursory remarks about the effect of roughness on the low-order modes.

Figure 18 shows that the effect of the surface roughness on the outer flow is quite pronounced. In the streamwise case, the presence of roughness in the simulation disrupts the alternating flow pattern found for the smooth case (figure 18*a*). By doing so, it decreases the size of the structures observed in the boundary layer. The typical length and width of structures in the smooth case are approximately 3δ and 0.5δ, whereas in the rough case the width is comparable but the length is only about δ. Furthermore, in the wall-normal velocity, the roughness has the effect of increasing

https://doi.org/10.1017/jfm.2013.326 Published online by Cambridge University Press

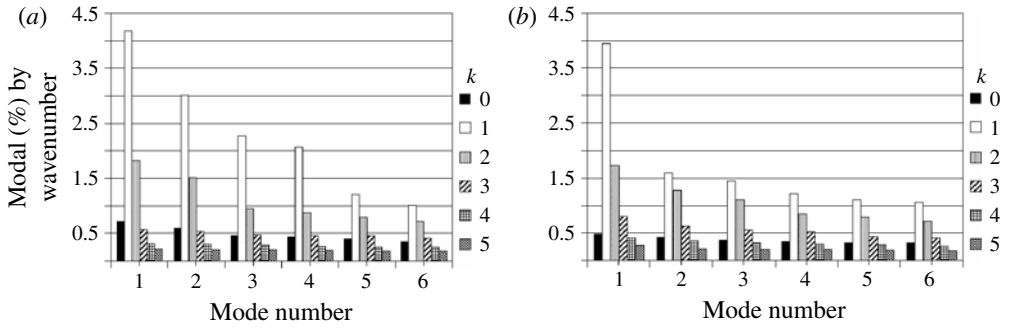


FIGURE 20. Turbulent kinetic energy content for POD modes 1–6 and wavenumbers 0–(±5) for (*a*) smooth and (*b*) rough.

the streamwise extent of injection events in the $k_z = 0, n = 1$ mode. For the smooth case, there are about five injection sites with a streamwise width of the order of $\delta_{inl}/4$. In the rough case there are still about five injection sites but the streamwise width is $O(3/4\delta_{inl})$. Thus, for injection sites that are similar in number and magnitude, the rough case will experience a greater volume of fluid injected from outside the boundary layer. For the spanwise velocity component, it may be observed that there are again alternating high- and low-speed regions. In both cases, these regions occur at an angle of 30° from the wall. A physical mechanism responsible for this inclination has not yet been explicitly identified. However, it is hypothesized that these angled structures contribute to hairpin vortices, as the angle observed here is comparable with the inclination angle associated with the flow structures, identified by Adrian, Meinhart & Tomkins (2000). The major difference between the smooth and rough cases for this velocity component is that in the smooth case, much longer high-speed regions are observed near the left and right ends of the domain, respectively.

Normalized eigenvalue spectra as a function of wavenumber and mode number for both smooth and rough cases are shown in figure 21, and turbulent kinetic energy (TKE) contributions based on wavenumber and mode number for both cases are summarized in figure 20(*a,b*). As may be observed from figure 21, for both the smooth and rough cases the eigenvalues decay faster with k_z than with n. This is to be expected since k_z accounts for variation in only one spatial direction while n accounts for variations in two spatial dimensions. Observation of the eigenvalue spectra in figures 21 and 20(*a,b*) indicates a redistribution of the TKE amongst the various length scales, with the most noticeable effects being for low wave and mode numbers. It can be observed from figure 20(*a,b*) that in the smooth case, there is more turbulent kinetic energy contribution in the first five wave and mode numbers than for the rough case. However, the opposite is true of the high wave/mode numbers; for these wave/mode numbers, there is more TKE contribution in the rough case than the smooth. These effects are most easily seen in figure 21(*b*). Here the eigenvalues (as a function of mode number) are shown for wavenumbers of $k_z = 1$ and $k_z = 19$. It may be observed that for the low-wavenumber, low-order smooth modes contain larger fractions of TKE than the rough modes, but that for higher mode numbers, the fractional contributions become nearly equivalent. For the high-wavenumber case, the rough modes have larger fractional contributions to the TKE for all mode numbers. This effect would seem to indicate that the presence of roughness leads to more energetic small-scale structures.

https://doi.org/10.1017/jfm.2013.326 Published online by Cambridge University Press

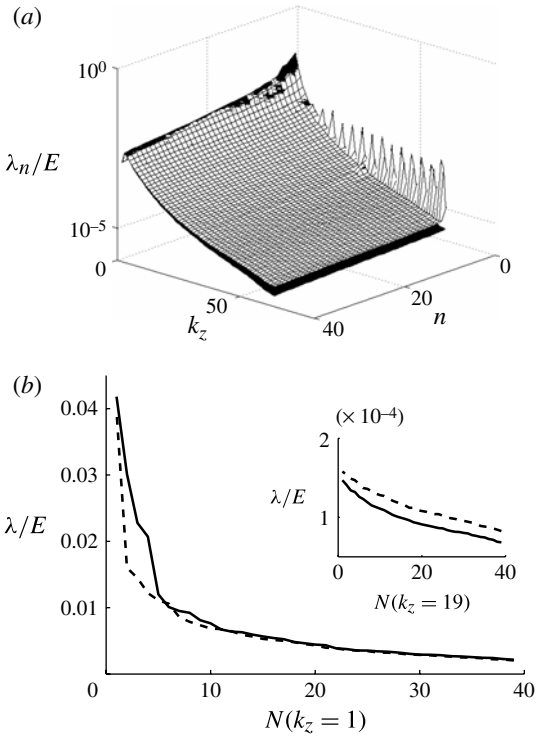


FIGURE 21. (*a*) Eigenvalue spectra for the smooth (black) and rough (white) cases, (*b*) Eigenvalues as a function of mode number for $k_z = 1$ and 19: ———, smooth λ; ------, rough λ.

7. Conclusions

The dynamic multi-scale approach has been successfully extended to incorporate rough surfaces and has saved valuable computational resources in simulating the turbulent boundary layer. Furthermore, a new methodology for simulating sand grit surface roughness in a CFD environment has been implemented. The new method involves using actual measurements of surface topography and importing these measurements onto a Cartesian mesh. The calculation of the Kolmogorov length scales has demonstrated that the mesh resolution is able to resolve the entire flow field for the smooth and rough cases. However, the mesh is marginally sufficient to fully resolve all the details of the sand grit surface topography, particularly in the streamwise direction where $\Delta x^+ \approx 24.6$ is marginally sufficient. Furthermore, the new methodology can be significantly improved in accuracy by implementing a higher-order immersed boundary method.

Comparisons of the numerical results with experiments performed under similar conditions show good agreement. The boundary layer parameters were reasonably close to the accepted experimental results of Brzek *et al.* (2008) and Schultz & Flack (2003). With regard to the wall shear stress, the numerical results were within 3 % of the experimental data, which is very convincing considering that there were some slight differences in the Reynolds number and roughness parameter.

The numerical results for the velocity field were also very promising. The iso-contours for the instantaneous velocity field qualitatively demonstrated that the

https://doi.org/10.1017/jfm.2013.326 Published online by Cambridge University Press

presence of surface roughness caused an overall thickening of the turbulent boundary layer in addition to modifying the streamwise structures of the turbulent boundary layer. Furthermore, changes in the instantaneous velocity field could be seen well beyond the inner region of the boundary layer, as enhanced mixing could be seen throughout the entire boundary layer. Based on observation of the iso-contours, the current recycling method did not introduce any periodicity to the flow. Quantitative comparison of the numerical results for the mean velocity field showed that the particular surface roughness under investigation caused a 4 % increase in the velocity deficit when compared to the smooth surface DNS results of Araya *et al.* (2009).

The effects of roughness on the Reynolds stresses are scale-dependent. In general and for the Reynolds number range considered here, it was observed that peak values of Reynolds stresses increased when considering outer units; however, decreases were seen when using inner units. In the outer region, the most significant differences between the present DNS smooth and rough cases were computed in the wall-normal component $\langle v'^2 \rangle$ of the Reynolds stresses and in the Reynolds shear stresses $\langle u'v' \rangle$. Furthermore, the two-point correlation analysis has revealed the suitability of the computational dimensions. Moreover, the effects of roughness on two-point correlations (R_{uu}, R_{vv} and R_{ww}) are clearly visible in the near-wall region at $y^+ = 5$. In the outer region, two-point correlations of the rough case appear to be slightly less correlated than the smooth case.

Further, comparison of the low-order POD modes from the smooth case with those generated by Baltzer *et al.* (2010) by analysing the DNS database of Wu & Moin (2010) and finding strong similarities therein provides more compelling evidence for the applicability of the dynamic multi-scale approach. Additionally, the presence of surface roughness has been shown to cause a redistribution of the kinetic energy amongst the POD modes. POD modes from the simulation with surface roughness contained less energy in low-order modes and more energy in high-order modes than the modes generated from the simulation without roughness. Furthermore, the surface roughness was shown to increase the size of injection events in the first mode of the wall-normal component, leading to the conclusion that the presence of roughness will enhance mixing between fluid inside and outside the boundary layer. Finally, low-order modes of the streamwise component have shown characteristic wavelengths in the order of 3δ in the smooth case, while the same modes for the rough case have exhibited characteristic wavelengths of the order of δ.

Acknowledgements

This research was supported by grants from NSF–CBET, grant 0829020, and the Office of Naval Research (Dr R. Joslin, programme manager). L.C. acknowledges support from ONR project N00014-09-1-1007 (Dr R. Joslin, programme manager). Computational resources were supplied by SCOREC (Scientific Computation Research Center) and CCNI (Computational Center for Nanotechnology Innovations) at Rensselaer Polytechnic Institute. G.A. acknowledges XSEDE for computational resources (project number CTS080012N). The authors thank Professor M. P. Schultz and K. A. Flack from the United States Naval Academy for providing data from their experiments and Dr O. Sahni for valuable insight.

Appendix A. Grid independence test

Two different meshes composed of linear hexahedral elements are tested in the smooth ZPG case. Both meshes are structured with equidistant points along the

https://doi.org/10.1017/jfm.2013.326 Published online by Cambridge University Press

Variables	Coarse mesh	Refined mesh
$N_x \times N_y \times N_z$	190 × 96 × 90	400 × 150 × 125
Number of points	1 641 600	7 500 000
Number of elements	1 597 995	7 371 924
Δx^+	45	23
Δy^+_{min}, Δy^+_{max}	0.5, 45	0.5, 25
Δz^+	15	11

TABLE 4. Characteristics of the meshes employed in smooth ZPG simulations.

streamwise (x) and spanwise (z) directions. The mesh is stretched in the wall-normal direction (y). More grid points are clustered near the wall. The main features of coarse and refined meshes are depicted in table 4, such as number of points along the directions, number of hexahedral elements and mesh resolution.

Figure 22 depicts the mean streamwise velocity, turbulence intensities and Reynolds shear stresses in wall units obtained in the coarse and refined meshes at $Re_\theta = 2239$. The mean streamwise velocity profiles expressed in wall units exhibit closely analogous behaviour for both meshes in figure 22(a). Nevertheless, the velocity fluctuation profiles show some differences in both meshes. In particular, it is more evident in peak values of u'^+_{rms}, as seen in figure 22(b). Furthermore, the strategy has been to initiate the numerical simulations with a rather coarse grid, and later to interpolate the flow solution onto the refined grid, saving considerable computational resources. Finally, all results shown in this paper were computed by means of the refined mesh.

Appendix B. Kolmogorov length/time scales

In this section, suitability of the mesh resolution and time step are demonstrated by means of the Kolmogorov length and time scale calculation. According to Moin & Mahesh (1998), the smallest resolved length scale in DNS should be of the order of the Kolmogorov length scale, η_k. The Kolmogorov length scale is defined as $\eta_k = (\nu^3/\epsilon)^{1/4}$, where ϵ is the average rate of energy dissipation per unit mass, and ν is the kinematic viscosity of the fluid. Table 5 shows the Kolmogorov length scales at five different wall distances for the smooth and rough DNS cases. Vertical locations have been selected in such a way as to explore the Kolmogorov length scales at critical points, such as very close to the wall, peak locations of fluctuations and outer region. The first wall distance is the distance where the smallest length scale or maximum dissipation ϵ^+ is observed in the computational domain (e.g. $y^+ = 0.5$ and 24 for the smooth and rough cases, respectively). One can observe that the presence of the roughness causes the maximum dissipation of turbulent kinetic energy to be offset further from the wall. In this paper the vertical axis origin is considered at $y = 0$ in both cases, which coincides with the smooth wall. Consequently, the minimum Kolmogorov length scale was observed at $y^+ \approx 24$ (computation not shown). Furthermore, it can be inferred that the mesh resolutions are of the order of η_k (i.e. $\Delta y < 10\eta_k$). Therefore, the grid points for the current mesh are sufficient to resolve even the smallest scales in the flow. However, the mesh for the rough DNS case may be marginally adequate to fully resolve all the details of the sand grit surface topography, particularly in the streamwise direction.

https://doi.org/10.1017/jfm.2013.326 Published online by Cambridge University Press

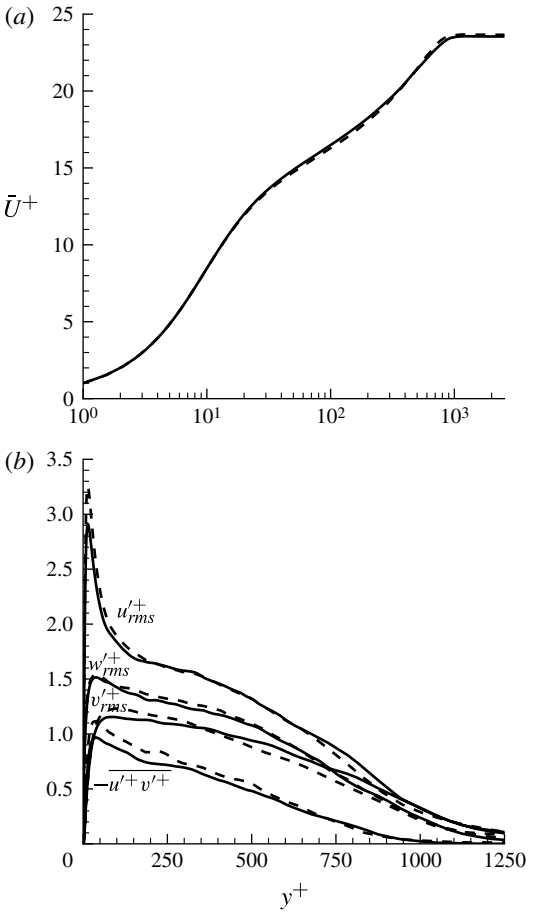


FIGURE 22. Grid independence test: (*a*) mean streamwise velocity and (*b*) turbulence intensities and Reynolds shear stresses at $Re_\theta = 2239$: - - - - - -, coarse mesh; ———, refined mesh.

Smooth DNS, $Re_\theta = 2239$				Rough DNS, $Re_\theta = 2278$			
y^+	$\lvert\epsilon^+\rvert$	η_k^+	Δy^+	y^+	$\lvert\epsilon^+\rvert$	η_k^+	Δy^+
0.5	0.45	1.22	0.50	24	0.8	1.06	1.36
5	0.31	1.34	0.65	30	0.25	1.41	1.56
15	0.29	1.36	1.0	40	0.17	1.56	1.93
40	0.15	1.63	1.93	65	0.1	1.78	2.76
500	0.0082	3.32	18.22	524	0.011	3.09	18.8

TABLE 5. Kolmogorov length scales.

Similarly, table 6 exhibits the Kolmogorov time scales at five different wall distances for the smooth and rough cases. The Kolmogorov time scale is defined as $\tau_\eta = (\nu/\epsilon)^{1/2}$. In the present study, the time steps are chosen by considering the Courant–Friedrichs–Lewy (CFL) parameters approximately equal to 0.5, which

https://doi.org/10.1017/jfm.2013.326 Published online by Cambridge University Press

Smooth DNS, $Re_\theta = 2239$				Rough DNS, $Re_\theta = 2278$			
y^+	$\lvert\epsilon^+\rvert$	τ_η^+	Δt^+	y^+	$\lvert\epsilon^+\rvert$	τ_η^+	Δt^+
0.5	0.45	1.491	0.44	24	0.8	1.118	0.5
5	0.31	1.796	0.44	30	0.25	2.0	0.5
15	0.29	1.857	0.44	40	0.17	2.425	0.5
40	0.14	2.673	0.44	65	0.1	3.162	0.5
500	0.0082	11.04	0.44	524	0.011	9.535	0.5

TABLE 6. Kolmogorov time scales.

results in accurate prediction of turbulence statistics. According to Choi & Moin (1995), 'turbulence fluctuations can only be sustained if the computational time step is appreciably less than the Kolmogorov time scale'. Clearly, it can be seen from table 6 that the selected time steps in wall units (i.e. Δt^+) are much lower than the corresponding dimensionless Kolmogorov time scales, τ_η^+, at all vertical coordinates considered for the smooth and rough cases.

REFERENCES

ADRIAN, R., MEINHART, C. & TOMKINS, C. 2000 Vortex organization in the outer region. *J. Fluid Mech.* **422**, 1–54.

ARAYA, G. & CASTILLO, L. 2012 DNS of turbulent thermal boundary layers up to $Re_\theta = 2300$. *Intl J. Heat Mass Transfer* **55**, 4003–4019.

ARAYA, G., CASTILLO, L. & JANSEN, K. 2013 DNS of stable spatially-developing turbulent thermal boundary layers under weak stratification. In *Springer Proceedings in Physics,* vol. 149, *Progress in Turbulence V* (ed. A. Talamelli, M. Oberlack & J. Peinke). Proceedings of the iTi Conference in Turbulence 2012, Springer.

ARAYA, G., CASTILLO, L., MENEVEAU, C. & JANSEN, K. 2011 A dynamic multi-scale approach for turbulent inflow boundary conditions in spatially evolving flows. *J. Fluid Mech.* **670**, 581–605.

ARAYA, G., JANSEN, K. & CASTILLO, L. 2009 Inlet condition generation for spatially developing turbulent boundary layers via multi-scale similarity. *J. Turbul.* **10** (36), 1–33.

AUBRY, N., GUYONNET, R. & LIMA, R. 1992 Spatio-temporal symmetries and bifurcations via bi-orthogonal decompositions. *J. Nonlinear Sci.* **2**, 183–215.

BALTZER, J., ADRIAN, R. & WU, X. 2010 Turbulent boundary layer structure identification via POD. Stanford Center for Turbulence Research Summer Program 2010, pp. 55–64.

BRZEK, B., BAILON-CUBA, J., LEONARDI, S. & CASTILLO, L. 2009 Theoretical evaluation of the Reynolds shear stress and flow parameters in transitionally rough turbulent boundary layers. *J. Turbul.* **10**, 1–28.

BRZEK, B., CAL, R. B., JOHANSSON, G. & CASTILLO, L. 2008 Transitionally rough zero pressure gradient turbulent boundary layers. *Exp. Fluids* **44**, 115–124.

CAL, R., BRZEK, B., JOHANSSON, T. & CASTILLO, L. 2009 The rough favourable pressure gradient turbulent boundary layer. *J. Fluid Mech.* **641**, 129–155.

CASTILLO, L. & JOHANSSON, G. 2002 The effects of upstream conditions on a low Reynolds number turbulent boundary layer with zero pressure gradient. *J. Turbul.* **3**, 1–19.

CHOI, H. & MOIN, P. 1995 Effects of the computational time step on numerical solutions of turbulent flow. *J. Comput. Phys.* **113**, 1–4.

CLAUSER, F. H. 1954 Turbulent boundary layers in adverse pressure gradients. *J. Aeronaut. Sci.* **21**, 91–108.

GEORGE, W. & CASTILLO, L. 1997 Zero-pressure-gradient turbulent boundary layer. *Appl. Mech. Rev.* **50**, 689–729.

https://doi.org/10.1017/jfm.2013.326 Published online by Cambridge University Press

GEORGE, J., SIMONE, A. D., IACCARINO, G. & JIMÉNEZ, J. 2010 Modelling roughness effects in turbulent boundary layers by elliptic relaxation. *Cent. Turbul. Res.* **36**, 119–128.

HAMA, F. R. 1945 Boundary-layer characteristics for smooth and rough surfaces. *Soc. Nav. Archit. Nav. Eng.* **62**, 333–358.

HOLMES, P., LUMLEY, J. & BERKOOZ, G. 1997 *Turbulence, Coherent Structures, Dynamical Systems and Symmetry*. Cambridge University Press.

HONG, J., KATZ, J. & SCHULTZ, M. 2011 Near-wall turbulence statistics and flow structures over three-dimensional roughness in a turbulent channel flow. *J. Fluid Mech.* **667**, 1–37.

JIMÉNEZ, J. 2004 Turbulent flows over rough walls. *Annu. Rev. Fluid Mech.* **36**, 173–196.

KHUJADZE, G. & OBERLACK, M. 2004 DNS and scaling laws from new symmetry groups of ZPG turbulent boundary layer flow. *Theor. Comput. Fluid Dyn.* **18**, 391–411.

KIM, J. & MOSER, R. 1987 Turbulence statistics in fully developed channel flow at low Reynolds number. *J. Fluid Mech.* **129**, 133–166.

KROGSTAD, P., ANTONIA, R. & BROWNE, L. W. B. 1992 Comparison between rough- and smooth-wall turbulent boundary layers. *J. Fluid Mech.* **245**, 599–617.

KROGSTAD, P.-A. & EFROS, V. 2012 About turbulence statistics in the outer part of a boundary layer developing over two-dimensional surface roughness. *Phys. Fluids* **24** (7), 075112.

KUNKEL, G. & MARUSIC, I. 2006 Study of the near-wall turbulent region of the high-Reynolds-number boundary layer using an atmospheric flow. *J. Fluid Mech.* **548**, 375–402.

LEONARDI, S., ORLANDI, P., SMALLEY, R., DJENIDI, L. & ANTONIA, R. 2003 Direct numerical simulations of turbulent channel flow with transverse square bars on one wall. *J. Fluid Mech.* **491**, 229–238.

LIU, Z.-C., ADRIAN, R. & HANRATTY, T. 2001 Large-scale models of turbulent channel flow: transport and structure. *J. Fluid Mech.* **448**, 53–80.

LUND, T., WU, X. & SQUIRES, K. 1998 Generation of turbulent inflow data for spatially-developing boundary layer simulations. *J. Comput. Phys.* **140**, 233–258.

MOIN, P. & MAHESH, K. 1998 Direct numerical simulation: a tool in turbulence research. *Annu. Rev. Fluid Mech.* **30**, 539–578.

MOIN, P. & MOSER, R. 1989 Characteristic-eddy decomposition of turbulence in a channel. *J. Fluid Mech.* **200**, 471–509.

NIKURADSE, J. 1933 Laws of flow in rough pipes. *NACA TM 1292*.

PERRY, A. & JOURBERT, P. 1963 Rough wall boundary layers in adverse pressure gradients. *J. Fluid Mech.* **17**, 193–211.

PERRY, A., LIM, K. & HENBEST, S. 1987 An experimental study of the turbulent structure in smooth- and rough-wall boundary layers. *J. Fluid Mech.* **177**, 437–466.

RAUPACH, M. 1991 Rough-wall turbulent boundary layers. *Appl. Mech. Rev.* **44**, 1–25.

ROTTA, J. C. 1960 Turbulent boundary layers with heat transfer in compressible flow. *AGARD Report* 281.

SCHLICHTING, H. 1979 *Boundary-Layer Theory*, 7th edn. McGraw-Hill.

SCHULTZ, M. & FLACK, K. 2003 Turbulent boundary layers over surfaces smoothed by sanding. *Trans. ASME: J. Fluids Engng* **125**, 863–870.

SCHULTZ, M. & FLACK, K. 2007 The rough-wall turbulent boundary layer from the hydraulically smooth to the fully rough regime. *J. Fluid Mech.* **580**, 381–405.

SCOTTI, A. 2007 Direct numerical simulation of turbulent channel flows with boundary roughened with virtual sandpaper. *Phys. Fluids* **18**, 031701.

SIMENS, M., JIMÉNEZ, J., HOYAS, S. & MIZUNO, Y. 2009 A high-resolution code for turbulent boundary layers. *J. Comput. Phys.* **228**, 4218–4231.

SIROVICH, L. 1987 Turbulence and the dynamics of coherent structures. Parts 1, 2 and 3. *Q. Appl. Maths* **XLV**, 561–590.

STOLZ, S. & ADAMS, N. A. 2003 Large-eddy simulation of high-Reynolds-number supersonic boundary layers using the approximate deconvolution model and a rescaling and recycling technique. *Phys. Fluids* **15**, 2398–2412.

SUN, C. 2008 Parallel algebraic multigrid for the pressure Poisson equation in a finite element Navier–Stokes solver. PhD dissertation, Rensselaer Polytechnic Institute.

https://doi.org/10.1017/jfm.2013.326 Published online by Cambridge University Press

TOWNSEND, A. 1976 *The Structure of Turbulent Shear Flow*. Cambridge University Press.

WHITE, F. M. 1974 *Viscous Fluid Flow*. McGraw-Hill.

WHITING, C. & JANSEN, K. 2001 A stabilized finite element method for incompressible Navier–Stokes equations using a hierarchical basis. *Intl J. Numer. Meth. Fluids* **35**, 93–116.

WU, X. & MOIN, P. 2010 Transitional and turbulent boundary layer with heat transfer. *Phys. Fluids* **22**, 085105.

https://doi.org/10.1017/jfm.2013.326 Published online by Cambridge University Press